On the numerical implementation of time-reversal mirrors for tomographic imaging

Yder Masson,[1] Paul Cupillard,[2] Yann Capdeville[3] and Barbara Romanowicz[4,1,5]

[1]*Institut de Physique du Globe, 1 Rue Jussieu F-75005, Paris, France. E-mail: masson@ipgp.fr*
[2]*Université de Lorraine, Laboratoire GéoRessources (UMR 7359), F-54500 Vandoeuvre-lès-Nancy, France*
[3]*LPGN, UFR Sciences et Techniques, Université de Nantes, F-44322 Nantes Cedex 3, France*
[4]*Collège de France, 11, Marcelin Berthelot F-75231 Paris Cedex 05, Paris, France*
[5]*Berkeley Seismological Laboratory, University of California, Berkeley, CA 94720, USA*

SUMMARY
A general approach for constructing numerical equivalents of time-reversal mirrors is introduced. These numerical mirrors can be used to regenerate an original wavefield locally within a confined volume of arbitrary shape. Though time-reversal mirrors were originally designed to reproduce a time-reversed version of an original wavefield, the proposed method is independent of the time direction and can be used to regenerate a wavefield going either forward in time or backward in time. Applications to computational seismology and tomographic imaging of such local wavefield reconstructions are discussed. The key idea of the method is to directly express the source terms constituting the time-reversal mirror by introducing a spatial window function into the wave equation. The method is usable with any numerical method based on the discrete form of the wave equation, for example, with finite difference (FD) methods and with finite/spectral elements methods. The obtained mirrors are perfect in the sense that no additional error is introduced into the reconstructed wavefields apart from rounding errors that are inherent in floating-point computations. They are fully transparent as they do not interact with waves that are not part of the original wavefield and are permeable to these. We establish a link between some hybrid methods introduced in seismology, such as wave-injection, and the proposed time-reversal mirrors. Numerical examples based on FD and spectral elements methods in the acoustic, the elastic and the visco-elastic cases are presented. They demonstrate the accuracy of the method and illustrate some possible applications. An alternative implementation of the time-reversal mirrors based on the discretization of the surface integrals in the representation theorem is also introduced. Though it is out of the scope of the paper, the proposed method also apply to numerical schemes for modelling of other types of waves such as electro-magnetic waves.

Key words: Numerical solutions; Numerical approximations and analysis; Tomography; Seismic tomography; Computational seismology; Wave propagation.

1 INTRODUCTION

The development of powerful computer clusters and efficient numerical computation methods, such as finite difference (FD), finite element (FE) and spectral element (SEM) methods has made it possible to compute seismic wave propagation in a heterogeneous 3-D Earth with unprecedented accuracy (e.g. Moczo *et al.* 2002; Dumbser *et al.* 2007; Peter *et al.* 2011; Cupillard *et al.* 2012). However, the cost of these computations is still problematic in many situations. For example, high-resolution imaging of the subsurface in exploration seismology or global scale Earth tomography require at least a few thousands of such wave propagation simulations. Hence,

part of the ongoing research effort is dedicated to the development of faster modelling methods for computing synthetic seismograms in a 3-D heterogeneous Earth. Capdeville *et al.* (2002, 2003) proposed to couple SEM simulations with normal modes calculation (C-SEM). Robertsson & Chapman (2000) proposed to limit the wave propagation calculations inside a subregion. Nissen-Meyer *et al.* (2007) used 2-D simulations to compute 3-D seismograms in a 1-D earth model. Capdeville, Guillot & Marigo (2010), Capdeville *et al.* (2013) and Fichtner *et al.* (2013) developed upscaling techniques to account for smaller scale heterogeneity at a reduced computational cost. Thanks to some of these developments, and for the first time, Lekić & Romanowicz (2011) and French *et al.*

(2013) developed 3-D global models of the upper mantle using SEM simulations. At the local and continental scale, full waveform inversions (e.g. adjoint tomography) that are using a large quantity of wave propagation simulations can be implemented on current generation computers (e.g. Bamberger *et al.* 1982; Chen *et al.* 2007; Fichtner *et al.* 2010; Tape *et al.* 2009; Rickers *et al.* 2012; Zhu *et al.* 2012; Rickers *et al.* 2013). Due to their smaller size, these models offer higher resolution. They provide us with images of the crust and the upper part of the mantle. In an attempt to extend such local full waveform inversions into the deep earth, we developed a numerical equivalent of time-reversal mirrors that permits to limit the wave propagation computation to a region of interest within the earth. This paper details the implementation of the proposed time-reversal mirror and discusses some possible applications.

Time-reversal, as introduced by Fink *et al.* (Fink 1992, 1997; Fink *et al.* 1989; Fink *et al.* 2001) and more recently applied to geophysical problems (e.g. Larmat *et al.* 2006; Larmat *et al.* 2008; Montagner *et al.* 2012) is a two-step process. First, waves propagating through a medium are recorded with an array of transducers. Then, the records are reversed in time and re-emitted by the transducers back into the medium, so that the wave energy is refocused in time and space at the position of the source. The refocusing property is due to the reciprocity in space and reversibility in time of the elastic/acoustic wave equation, provided that attenuation is negligible. The array of transducers used for time reversal is commonly referred to as a time-reversal mirror, or, as a time-reversal cavity, in the special case where it forms a closed surface. In theory, it is possible to regenerate the time reversed version of the original wavefield inside a time-reversal cavity by recording the wavefield and its gradient and re-emitting appropriate signals with the mirror's transducers. However, achieving a perfect reconstruction of the original wavefield experimentally is a difficult task due to physical limitations (Cassereau & Fink 1992). For example, recording both the wavefield and its gradient or generating arbitrary sources is not fully possible with available transducers. In addition, the energy refocusing at the source point needs to be canceled out using an acoustic sink in order to regenerate only the causal part of the wavefield. Last, in the case of dissipative media, the time symmetry is broken and regenerating the exact time-reversed version of the original wavefield is not possible. Hopefully, numerical methods do not suffer such limitations as arbitrary complex sources can be modelled. We will show that a perfect reconstruction of the original wavefield using numerical time-reversal mirrors is achievable in the acoustic, elastic, and to some extent in the visco-elastic case that is more delicate due to numerical instabilities (i.e. because the roundoff error is amplified with the wavefield).

Though they are not always referred as such, time-reversal mirrors are used and have some important applications in computational seismology. For example, the computation of sensitivity kernels in full waveform inversion (e.g. Bamberger *et al.* 1982; Tarantola 1984; 1988; Tromp *et al.* 2005; Fichtner *et al.* 2006; Plessix 2006; Liu & Tromp 2008; Chen 2011) or reverse time migration (Baysal *et al.* 1983; Whitmore 1983; Biondi & Shan 2002; Yoon *et al.* 2003, 2004; Mulder & Plessix 2004; Bednar *et al.* 2006) requires to have simultaneous access to both the forward wavefield (e.g. the wavefield generated by an earthquake) at time $T - t$ (where T is the duration of the simulations) and a time-reversed wavefield at time t (e.g. the back propagation of the difference between the observed seismogram and the synthetic seismogram computed in the forward calculation). Such a simultaneous access is unachievable when the

forward simulation and the adjoint simulation are run simultaneously in the time domain. One solution is to first run the forward simulation and save the entire wavefield versus time and space so its values can be later recovered at the desired instant, when running the adjoint simulation. While it has been sucessfully implemented by subsampling the forward wavefield (e.g. Fichtner *et al.* 2009), this approach requires a significant amount of disk space. Another elegant approach that greatly reduces the storage requirement is to use an extra simulation where the time reversed version of the forward wavefield is regenerated (e.g. Gauthier *et al.* 1986; Akcelik *et al.* 2003; Liu & Tromp 2006, 2008). That operation requires a numerical equivalent of a time-reversal mirror. In that case, two simulations are being run in parallel (i.e. the adjoint simulation and the time-reversed simulation), both wavefields are known simultaneously at the desired instant, and the adjoint sensitivity kernel can be computed on the fly, provided that dissipation is sufficiently weak. Alternatives strategies for limiting the memory usage are discussed in, for example Symes (2007). Alternative methods such as random boundaries or time-varying boundaries have also been introduced to back propagate a forward wavefield in parallel with the adjoint simulation (e.g. Clapp 2009; Fletcher & Robertsson 2011).

As their name suggests, time-reversal mirrors were originally thought to propagate a wavefield backward in time, however, thanks to the time-reversal invariance of the wave equation, these tools can be used equally to propagate a similar wavefield forward in time. Used in such a manner, time-reversal mirrors relate to numerous so-called hybrid methods or domain decomposition methods that have been introduced in seismology. Hybrid methods generally divide the computational domain into two domains in which wave propagation is computed separately, often with different methods. A larger volume where wave propagation is computed in a background model and a smaller volume encompassed by the first one and containing the object responsible for the scattered waves of interest. Various hybrid methods are presented in, for example Alterman & Karal 1968; Bielak & Christiano 1984; Bielak *et al.* 2003; Bouchon & Sanchez-Sesma 2007; Capdeville *et al.* 2002, 2003; Godinho *et al.* 2009; Moczo *et al.* 1997; Monteiller *et al.* 2013; Opršal *et al.* 2009; Robertsson & Chapman 2000; To *et al.* 2005; Wen & Helmberger 1998; Yoshimura *et al.* 2003; Zhao *et al.* 2008. The motivation behind hybrid methods is that approximate solutions for wave propagation and/or simpler (e.g. 1-D) background models may be used in the larger volume while exact wave propagation computations can be limited to the inner volume. This allows for very efficient computation of the wavefield due to scatterers that are localized in a specific region. Hybrid methods divide into two categories, real time methods, where boundary conditions are exchanged rapidly (e.g. Capdeville *et al.* 2002) and two-step methods, where wave propagation is first performed in the background model and then used as an input to obtain the wavefield inside the inner volume (e.g. Robertsson & Chapman 2000). Although often treated as boundary condition problems, the methods falling into the second category can interestingly be thought as a specific use of, and implemented with, time-reversal mirrors. In that case, instead of imposing boundary conditions at the surface of a given volume, an equivalent excitation source is used to inject the wavefield into it. We will show, for example that the wave injection method proposed by Robertsson & Chapman (2000) can be seen as an exact numerical equivalent of a time-reversal mirror.

In the acoustic case, the ideal response of a time-reversal mirror can be expressed formally in the frequency domain with the

Helmoltz-Kirchhoff representation theorem (e.g. Cassereau & Fink 1992; Fink & Prada 2000)

$$p^*(\mathbf{x}) = \oint_S \frac{1}{\rho} \left(G(\mathbf{x}, \mathbf{x}') \nabla p^*(\mathbf{x}') - p^*(\mathbf{x}') \nabla G(\mathbf{x}, \mathbf{x}') \right) \cdot d S, \qquad (1)$$

where p is the acoustic pressure, ρ is density, G is the Green's function and the star symbol ($*$) denotes the complex conjugate. In the elastic case, and when accounting for the acoustic sink needed to cancel out the energy refocusing at the source location, the response can be expressed using the representation theorem (e.g. De Hoop 1958; Aki 1980; Snieder 2002)

$$u_i^*(\mathbf{x}) = \int_V G_{in}(\mathbf{x}, \mathbf{x}') f_n^*(\mathbf{x}') \, d V'$$

$$+ \oint_S G_{in}(\mathbf{x}, \mathbf{x}') n_j C_{njkl} \partial_k' u_l^*(\mathbf{x}') \, d S'$$

$$- \oint_S u_n^*(\mathbf{x}') n_j C_{njkl} \partial_k' G_{il}(\mathbf{x}, \mathbf{x}') \, d S', \qquad (2)$$

where u is the displacement vector, the Green's tensor, $G_{in}(\mathbf{x}, \mathbf{x}')$, denotes the displacement at location $\mathbf{x}$ in the i direction due to a unit point force at $\mathbf{x}'$ in the n direction, $C_{ijkl} = C_{ijkl}(\mathbf{x})$ is the elasticity tensor and the notation ∂_k' stands for the derivative with respect to the x_k' coordinate: $\partial_k' f \equiv \partial f / \partial x_k'$. Eq. (2) means that, if the exciting force $f_n(\mathbf{x}')$ is known throughout the volume V, and the wavefield $u_n(\mathbf{x}')$ and the associated traction $n_j C_{ijkl} \partial_k' u_l(\mathbf{x}')$ are known on the surface S, we have enough information to regenerate the wavefield everywhere within the volume V. Practically, the construction of an elastic time-reversal mirror consists in determining the excitation source that, applied on the surface S, will generate the response in eq. (2), that is that will regenerate the original wavefield inside the volume V.

In Section (2), we show that the mirror's excitation source can be directly expressed by introducing a spatial window function into the wave equation. We show that, in the special case where the window function is bi-valued (i.e. it is either equal to zero or one), the response of the proposed excitation source satisfies the representation theorem in eq. (2). In Section (3), we propose a general method for implementing the proposed time-reversal mirrors numerically. We detail the numerical scheme obtained when using FD methods and the FE/SEMs methods. An alternative implementation based on a direct discretization of the surface integrals in eq. (2) is introduced in Section (3.2). In Section (5), we present numerical examples demonstrating the accuracy of the proposed methods and illustrating some possible applications.

2 DERIVATION OF THE ELASTIC MIRROR

In this section, we show that the mirror's excitation force can be naturally expressed by inserting the local version of the original wavefield that we want to regenerate (see eq. 5) into the wave equation. Practically, this involves applying a spatial window function to the original wavefield. We demonstrate that, when the window function employed defines a closed subvolume, the response to the obtained mirror's excitation is given by the representation theorem in eq. (2). Consider a displacement wavefield $\mathbf{u}(\mathbf{x}, t)$ in an arbitrary volume V that is a solution of the wave equation

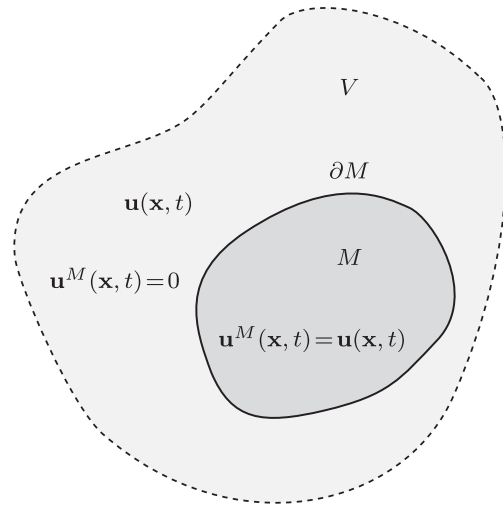$$\rho \ddot{u}_n - \partial_j \left(C_{njkl} \partial_k u_l \right) = f_n. \qquad (3)$$

Figure 1. For an arbitrary wavefield $\mathbf{u}$ defined in a general volume V, we want to generate the wavefield $\mathbf{u}^M$ that is equal to $\mathbf{u}$ inside a subvolume M encompassed in V and zero elsewhere.

In the frequency domain, eq. (3) is

$$\rho \omega^2 u_n + \partial_j \left(C_{njkl} \partial_k u_l \right) = -f_n. \qquad (4)$$

Our goal is to construct a mirror or excitation force field that regenerates the wavefield $\mathbf{u}^M(\mathbf{x}, t)$ within a subvolume $M \in V$ bounded by a closed surface ∂M so that

$$\mathbf{u}^M(\mathbf{x}, t) = \begin{cases} \mathbf{u}(\mathbf{x}, t) & \text{for all} \quad \mathbf{x} \in M \\ 0 & \text{for all} \quad \mathbf{x} \notin M \end{cases}, \qquad (5)$$

as pictured in Fig. 1. The wavefield $\mathbf{u}^M$ can be expressed as

$$\mathbf{u}^M(\mathbf{x}, t) = \mathbf{u}(\mathbf{x}, t) w(\mathbf{x}), \qquad (6)$$

where w is a time-independent window function. In this section, we consider the situation where w is bi-valued, that is we have

$$w(\mathbf{x}) = \begin{cases} 1 & \text{for all} \quad \mathbf{x} \in M \\ 0 & \text{for all} \quad \mathbf{x} \notin M \end{cases}. \qquad (7)$$

Note that the window function w as defined in eq. (7) is not differentiable in the classic sense, however, its derivative may be expressed in terms of Dirac's delta distributions. The function w may also be approximated with, and thought as, an arbitrary continuous function that is gradually varying from zero to one in the vicinity of ∂M. Assuming that, the local wavefield $\mathbf{u}^M$ is differentiable in time and space, we now introduce the force field

$$f_n^M = -\rho \omega^2 u_n^M - \partial_j \left(C_{njkl} \partial_k u_l^M \right), \qquad (8)$$

which is by definition the mirror's excitation force field that generates $\mathbf{u}^M$. Inserting $u_n^M = w u_n$ in eq. (8) and replacing $\rho \omega^2 u_n$ with its value from eq. (4) we obtain

$$f_n^M = w \partial_j \left(C_{njkl} \partial_k u_l \right) + w f_n - \partial_j \left(C_{njkl} \partial_k w u_l \right), \qquad (9)$$

or, after developing and simplifying

$$f_n^M = w f_n - C_{njkl} \partial_j w \partial_k u_l - \partial_j (u_l C_{njkl} \partial_k w). \qquad (10)$$

When the original wavefield $\mathbf{u}(\mathbf{x}, t)$ is known in the vicinity of ∂M, the exciting force $\mathbf{f}^M$ can be obtained by evaluating the right-hand side of eqs (8)–(10). In the next section, we show that a discrete equivalent of eq. (9) allows for a straightforward implementation of the mirror.
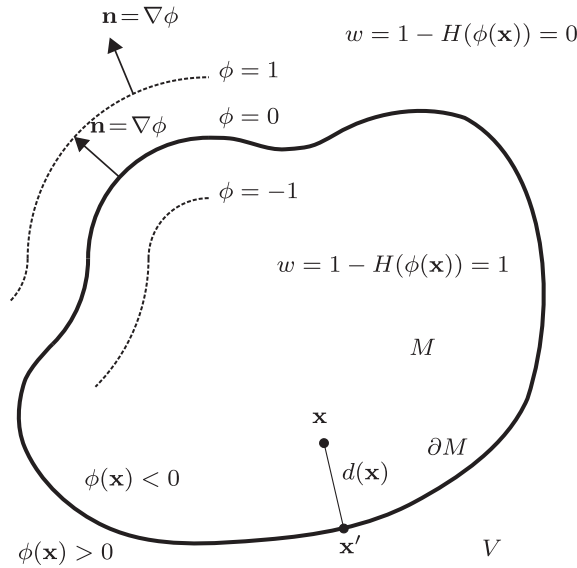
Figure 2. The distance function $d(\mathbf{x})$ expresses the minimum distance form a point $\mathbf{x}$ to the surface ∂M. The signed distance function $\Phi(\mathbf{x})$ shares the same absolute value with $d(\mathbf{x})$ but it is, respectively, negative and positive inside and outside the volume M. The window function w is defined implicitly as a function of $\Phi(\mathbf{x})$, it is equal to one inside volume M and zero outside.

We now show that the response $\mathbf{u}^M$ at location $\mathbf{x}$ due to the mirror's excitation $\mathbf{f}^M$ in eqs (8)–(10) is indeed given by the representation theorem in eq. (2). The response $\mathbf{u}^M$ can be expressed formally by convolving the exciting force $\mathbf{f}^M$ in eq. (9) with the Green's function $\mathbf{G}(\mathbf{x}, \mathbf{x}')$ of the medium and integrating over volume, that is we have

$$u_i^M(\mathbf{x}) = \int_V G_{in}(\mathbf{x}, \mathbf{x}') f_n^M(\mathbf{x}') \, dV'. \tag{11}$$

For the sake of clarity, before we evaluate eq. (11), we first explicit w using implicit functions. At a given point $\mathbf{x} \in M$, the distance to the surface ∂M can be expressed as

$$d(\mathbf{x}) = \min\left(|\mathbf{x} - \mathbf{x}''|\right) \quad \text{for all} \quad x'' \in \partial M, \tag{12}$$

and the signed distance function $\phi(\mathbf{x})$ can be defined as

$$\phi(\mathbf{x}) = \begin{cases} -d(\mathbf{x}) & \text{for all} \quad \mathbf{x} \in M \\ d(\mathbf{x}) & \text{for all} \quad \mathbf{x} \notin M \\ d(\mathbf{x}) = 0 & \text{for all} \quad \mathbf{x} \in \partial M \end{cases}. \tag{13}$$

Notice that, as d is the Euclidian distance, we have $|\nabla \phi| = |\nabla d| = 1$ and the normal vector $\mathbf{n}$ to the surface ∂M is $\mathbf{n} = \nabla \phi$, or, using index notation $n_i = \partial_i \phi$. A graphical representation of the functions $d(\mathbf{x})$ and $\phi(\mathbf{x})$ is pictured in Fig. 2. The window function w can now be defined implicitly using the 1-D Heaviside function $H(x)$ as

$$w(\mathbf{x}) = 1 - H\left(\phi(\mathbf{x})\right), \tag{14}$$

and its gradient is

$$\partial_i w(\mathbf{x}) = -\delta\left(\phi(\mathbf{x})\right) n_i. \tag{15}$$

As an example, in the case of a volume within a spherical shell of radius one centred at the origin, one can use

$$\phi(\mathbf{x}) = \sqrt{x^2 + y^2 + z^2} - 1. \tag{16}$$

We now have all the ingredients to evaluate the response $\mathbf{u}^M$ in eq. (11). Inserting eq. (10) into eq. (11) gives

$$u_i^M(\mathbf{x}) = \int_V w(\mathbf{x}') G_{in}(\mathbf{x}, \mathbf{x}') f_n(\mathbf{x}') \, dV'$$

$$- \int_V G_{in}(\mathbf{x}, \mathbf{x}') \partial_j' w(\mathbf{x}') C_{njkl} \partial_k' u_l(\mathbf{x}') \, dV'$$

$$- \int_V G_{in}(\mathbf{x}, \mathbf{x}') \partial_j' \left[u_l(\mathbf{x}') C_{njkl} \partial_k' w(\mathbf{x}') \right] dV'. \tag{17}$$

When applying Gauss's theorem to the last term on the right-hand side of eq. (17), we obtain

$$\int_V G_{in}(\mathbf{x}, \mathbf{x}') \partial_j' \left[u_l(\mathbf{x}') C_{njkl} \partial_k' w(\mathbf{x}') \right] dV'$$

$$= \int_V \partial_j' \left[G_{in}(\mathbf{x}, \mathbf{x}') u_l(\mathbf{x}') C_{njkl} \partial_k' w(\mathbf{x}') \right] dV'$$

$$- \int_V \partial_j' G_{in}(\mathbf{x}, \mathbf{x}') u_l(\mathbf{x}') C_{njkl} \partial_k' w(\mathbf{x}') dV'$$

$$= \oint_S n_j G_{in}(\mathbf{x}, \mathbf{x}') u_l(\mathbf{x}') C_{njkl} \partial_k' w(\mathbf{x}') dS'$$

$$- \int_V \partial_j' G_{in}(\mathbf{x}, \mathbf{x}') u_l(\mathbf{x}') C_{njkl} \partial_k' w(\mathbf{x}') dV'$$

$$= - \int_V \partial_j' G_{in}(\mathbf{x}, \mathbf{x}') u_l(\mathbf{x}') C_{njkl} \partial_k' w(\mathbf{x}') dV', \tag{18}$$

where the surface integral vanishes because the integrand is compactly supported on ∂M, that is because V can be arbitrary large, the surface ∂M on which $\partial_k' w(\mathbf{x}') \neq 0$ can be assumed to be strictly inside S. Inserting eq. (18) into eq. (17), we obtain

$$u_i^M(\mathbf{x}) = \int_V w(\mathbf{x}') G_{in}(\mathbf{x}, \mathbf{x}') f_n(\mathbf{x}') dV'$$

$$- \int_V G_{in}(\mathbf{x}, \mathbf{x}') \partial_j' w(\mathbf{x}') C_{njkl} \partial_k' u_l(\mathbf{x}') \, dV'$$

$$+ \int_V \partial_j' G_{in}(\mathbf{x}, \mathbf{x}') u_l(\mathbf{x}') C_{njkl} \partial_k' w(\mathbf{x}') \, dV'. \tag{19}$$

Finally, substituting the indices j with k and n with l in the last integral on the right-hand side, using the stiffness tensor symmetry $C_{njkl} = C_{lkjn}$ and using the identities $\int_V w(\mathbf{x}) g(\mathbf{x}) dV = \int_M g(\mathbf{x}) dV$ and $\int_V g(\mathbf{x}) \partial_i w(\mathbf{x}) dV = -\int_V g(\mathbf{x}) \partial_i H\left(\phi(\mathbf{x})\right) dV = -\int_V g(\mathbf{x}) n_i \delta\left(\phi(\mathbf{x})\right) dV = -\oint_{\partial M} g(\mathbf{x}) n_i dS$, we obtain the representation theorem in its classic form

$$u_i^M(\mathbf{x}) = \int_M G_{in}(\mathbf{x}, \mathbf{x}') f_n(\mathbf{x}') dV'$$

$$+ \oint_{\partial M} G_{in}(\mathbf{x}, \mathbf{x}') n_j C_{njkl} \partial_k' u_l(\mathbf{x}') dS'$$

$$- \oint_{\partial M} u_n(\mathbf{x}') n_j C_{njkl} \partial_k' G_{il}(\mathbf{x}, \mathbf{x}') dS'. \tag{20}$$

The response in eq. (2) is simply obtained by substituting the complex conjugate of the wavefield (phase-conjugation being equivalent to time-reversal), its gradient and its sources into eq (20). Interestingly, we derived the representation theorem without invoking reciprocity. We showed that inserting a spatial window function into the wave equation allows to naturally express the mirror's excitation. In the situation where the window function defines a closed subvolume, the response to the mirror's excitation is given by the representation

theorem. In the next section, we adopt a similar approach based on the discrete version of the wave equation to construct a numerical equivalent of a time reversal mirror.

3 NUMERICAL METHOD

3.1 Direct discrete differentiation method

3.1.1 General displacement formulation

In this section, we start with the discrete wave equation and follow the same procedure as in Section 2 to construct the discrete equivalent of the mirror's excitation. The obtained expressions are general in the sense that they can be used along with any numerical method solving the discrete wave equation. The proposed expressions for the mirror's excitation permit an exact reconstruction of the original wavefield. The approach presented in this section allows to construct time-reversal mirrors having complex geometry, as, the surface on which the mirror acts, is implicitly defined by a spatial window function.

Practically, the numerical reconstruction of an original wavefield on a subgrid involves two successive steps. First, the excitation force field in eqs (8) and (9) needs to be computed versus time. Then, the induced response in eq. (11) is computed in the region of interest. In this section, we assume that both operations are performed using the same numerical method on identical meshes. However, in the perspective of practical applications, it is important to keep in mind that the excitation force field may be obtained using any other numerical method or analytical solution provided that the wavefield can be computed exactly in the desired background model and interpolated at the grid points.

In order to solve the wave equation numerically, it first needs to be discretized. Regardless of the method, the discrete equivalent of eq. (3) can be written in the general form (e.g. Hughes 1987; Fichtner 2010)

$$\mathbf{M} \cdot \ddot{\bar{\mathbf{u}}} + \mathbf{K} \cdot \bar{\mathbf{u}} = \bar{\mathbf{f}}, \tag{21}$$

where $\mathbf{M}$ and $\mathbf{K}$ are the *mass matrix* and the *stiffness matrix*, respectively, and the vector $\bar{\mathbf{u}}(t)$ usually contains the discrete values of the wavefield $\mathbf{u}(\mathbf{x}, t)$ evaluated at the grid points or some related expansion coefficients. Suppose that, using a first simulation, we solve the linear system in eq. (21) within an arbitrary volume for an excitation $\bar{\mathbf{f}}$. We then want to regenerate the discrete approximation $\bar{\mathbf{u}}^M(t)$ of the local wavefield $\mathbf{u}^M(t) = w\mathbf{u}(t)$ that is equal to $\mathbf{u}$ inside a subvolume M and zero outside. One obvious way to proceed is to record $\bar{\mathbf{u}}(t)$ versus time and space during the first simulation so its values can be recovered afterwards to obtain $\bar{\mathbf{u}}^M(t)$. Another approach is to construct a mirror excitation $\bar{\mathbf{f}}^M$ that satisfies

$$\mathbf{M} \cdot \ddot{\bar{\mathbf{u}}}^M + \mathbf{K} \cdot \bar{\mathbf{u}}^M = \bar{\mathbf{f}}^M. \tag{22}$$

and to perform a second simulation that solves the linear system in eq. (21) where the source term $\mathbf{f}$ has been replaced by $\mathbf{f}^M$. In order to compute the excitation $\bar{\mathbf{f}}^M$ one can define a general matrix $\bar{\mathbf{W}}$ that acts as the window function w in eq. (5) in the sense that it satisfies

$$\bar{\mathbf{u}}^M(t) = \bar{\mathbf{W}} \cdot \bar{\mathbf{u}}(t). \tag{23}$$

Inserting eq. (23) into eq. (22) gives an explicit expression for $\bar{\mathbf{f}}^M$ that depends only on the values $\bar{\mathbf{u}}$ computed during the first simulation, we have

$$\bar{\mathbf{f}}^M = \mathbf{M} \cdot \left(\bar{\mathbf{W}} \cdot \ddot{\bar{\mathbf{u}}} \right) + \mathbf{K} \cdot \left(\bar{\mathbf{W}} \cdot \bar{\mathbf{u}} \right). \tag{24}$$

One advantage of using eq. (24) along with an extra simulation as opposed to recording the full wavefield lies in the fact that the matrices $\mathbf{M}$ and $\mathbf{K}$ are usually sparse. This is because most numerical methods use basis functions with compact spatial support. Due to this, $\bar{\mathbf{f}}^M$ is zero at most grid nodes and one only needs to store its value at a few grid nodes. Note, however, that this is not necessarily the case for methods using high-order operators to evaluate the discrete spatial derivatives. We now consider, for a moment, the case where the matrix $\bar{\mathbf{W}}$ is diagonal and bi-valued, that is its off diagonal elements are zero and its diagonal elements are either equal to zero or one. For example, assuming the vector component $\bar{u}_i$ contains the displacement value at the grid node i, we have: $\bar{W}_{ii} = 1$ for the nodes i belonging to a subgrid where we want to reconstruct the wavefield and $W_{ij} = 0$ elsewhere. In that situation, in order to evaluate $\bar{\mathbf{f}}^M$ using eq. (24) one only needs to know the displacement $\bar{\mathbf{u}}$ and its time derivative $\ddot{\bar{\mathbf{u}}}$ recorded at grid points inside the subvolume or subgrid where we want to reconstruct the wavefield. Interestingly, by subtracting eq. (21) from eq. (24), it is possible to express $\bar{\mathbf{f}}^M$ as

$$\bar{\mathbf{f}}^M = \bar{\mathbf{f}} - \mathbf{M} \cdot \left[(\mathbf{I} - \bar{\mathbf{W}}) \cdot \ddot{\bar{\mathbf{u}}} \right] - \mathbf{K} \cdot \left[(\mathbf{I} - \bar{\mathbf{W}}) \cdot \bar{\mathbf{u}} \right]. \tag{25}$$

In this case, in contrast to eq. (24), one only needs to know the displacement $\bar{\mathbf{u}}$ and its time derivative $\ddot{\bar{\mathbf{u}}}$ recorded at grid points outside the subgrid where we want to reconstruct the wavefield. It is important to observe that two complementary sets of coefficients (e.g. corresponding to the wavefield values recorded at nodes inside and outside the subgrid of interest) contain the exact same information needed to regenerate the original wavefield inside the subdomain. As we will soon see, depending on the situation, using either eq. (24) or eq. (25) to compute $\bar{\mathbf{f}}^M$ can be more efficient computationally even though both expressions are exactly equivalent. In the situation where $\ddot{\bar{\mathbf{u}}}$ cannot be obtained because the past and/or futures values of $\bar{\mathbf{u}}$ are not known (e.g. at the beginning and the end of the simulation), it is possible to insert

$$\ddot{\bar{\mathbf{u}}} = \mathbf{M}^{-1} \left(\bar{\mathbf{f}} - \mathbf{K} \cdot \bar{\mathbf{u}} \right) \tag{26}$$

in eqs (24) and (25) to obtain an expression that only depends on the wavefield $\bar{\mathbf{u}}$ evaluated at the current time. In the desirable situation where both $\mathbf{W}$ and $\mathbf{M}$ are diagonal, eq. (24) becomes

$$\bar{\mathbf{f}}^M = \bar{\mathbf{W}} \cdot \bar{\mathbf{f}} - \bar{\mathbf{W}} \cdot (\mathbf{K} \cdot \bar{\mathbf{u}}) + \mathbf{K} \cdot \left(\bar{\mathbf{W}} \cdot \bar{\mathbf{u}} \right), \tag{27}$$

and eq, (25) becomes

$$\bar{\mathbf{f}}^M = \bar{\mathbf{W}} \cdot \bar{\mathbf{f}} + (\mathbf{I} - \bar{\mathbf{W}}) \cdot (\mathbf{K} \cdot \bar{\mathbf{u}}) - \mathbf{K} \cdot \left[(\mathbf{I} - \bar{\mathbf{W}}) \cdot \bar{\mathbf{u}} \right]. \tag{28}$$

In summary, either one of eqs (24)–(28) can be used to compute the mirror excitation $\bar{\mathbf{f}}^M(t)$. The simplest strategy to regenerate the wavefield $\bar{\mathbf{u}}^M(t)$ inside a subvolume M is to solve the linear system in eq. (21) using a first simulation. During that simulation, while the values of $\bar{\mathbf{u}}(t)$ are known, the source term $\bar{\mathbf{f}}^M(t)$ can be computed and stored. Then, the linear system in eq. (22) is solved in a second simulation using the appropriate mirror source $\bar{\mathbf{f}}^M$. As we will soon see, computing $\bar{\mathbf{f}}^M(t)$ explicitly during the first simulation is often not needed. In most cases, it is better to store the values of the wavefield $\bar{\mathbf{u}}$ at appropriate grid nodes.

3.1.2 Split formulation

In some situations, depending on the numerical method employed, it is more convenient to work with a split formulation of the discrete wave equation. For example, the displacement-stress formulation

$$\mathbf{M} \cdot \ddot{\bar{\mathbf{u}}} + \mathbf{K}_1 \cdot \bar{\sigma} = \bar{\mathbf{f}}, \tag{29}$$

$$\bar{\sigma} - \mathbf{K}_2 \cdot \bar{\mathbf{u}} = \bar{\mathbf{T}}, \tag{30}$$

or the velocity-stress formulation

$$\mathbf{M} \cdot \dot{\bar{\mathbf{v}}} + \mathbf{K}_1 \cdot \bar{\sigma} = \bar{\mathbf{f}}, \tag{31}$$

$$\dot{\bar{\sigma}} - \mathbf{K}_2 \cdot \bar{\mathbf{v}} = \dot{\bar{\mathbf{T}}}, \tag{32}$$

where $\mathbf{v}$ is the discrete approximation of the velocity vector, $\bar{\sigma}$ is the discrete approximation of the stress tensor, $\mathbf{K}_1$ and $\mathbf{K}_1$ are called stiffness matrices, by extension, and, $\bar{\mathbf{f}}$ and $\bar{\mathbf{T}}$ are the discrete approximations of a vector source and a tensor source, respectively. For these split-schemes, it is more appropriate (but not necessary) to apply the spatial window w to all fields involved in the calculation. For example, when using the velocity-stress formulation, one can define the matrices $\mathbf{W}_1$ and $\mathbf{W}_2$ using the identities

$$\bar{\sigma}^M(t) = \bar{\mathbf{W}}_1 \cdot \bar{\sigma}(t), \tag{33}$$

$$\bar{\mathbf{v}}^M(t) = \bar{\mathbf{W}}_2 \cdot \bar{\mathbf{v}}(t), \tag{34}$$

where, $\bar{\sigma}^M(t)$ and $\bar{\mathbf{v}}^M(t)$ are the discrete approximation of the local wavefields $\sigma^M(t) = w\sigma(t)$ and $\mathbf{v}^M(t) = w\mathbf{v}$, respectively. Inserting eqs (33) and (34) into eqs (31) and (32), respectively, leads to the mirror excitations

$$\bar{\mathbf{f}}^M = \mathbf{M} \cdot \left(\bar{\mathbf{W}}_2 \cdot \dot{\bar{\mathbf{v}}} \right) + \mathbf{K}_1 \cdot \left(\bar{\mathbf{W}}_1 \cdot \bar{\sigma} \right), \tag{35}$$

$$\dot{\bar{\mathbf{T}}}^M = \bar{\mathbf{W}}_1 \cdot \dot{\bar{\sigma}} - \mathbf{K}_2 \cdot \left(\bar{\mathbf{W}}_2 \cdot \bar{\mathbf{v}} \right), \tag{36}$$

or, when subtracting eqs (31) and (32) from eqs (35) and (36), respectively,

$$\bar{\mathbf{f}}^M = \bar{\mathbf{f}} - \mathbf{M} \cdot \left[(\mathbf{I} - \bar{\mathbf{W}}_2) \cdot \dot{\bar{\mathbf{v}}} \right] - \mathbf{K}_1 \cdot \left[(\mathbf{I} - \bar{\mathbf{W}}_1) \cdot \bar{\sigma} \right], \tag{37}$$

$$\dot{\bar{\mathbf{T}}}^M = \dot{\bar{\mathbf{T}}} - (\mathbf{I} - \bar{\mathbf{W}}_1) \cdot \dot{\bar{\sigma}} + \mathbf{K}_2 \cdot \left[(\mathbf{I} - \bar{\mathbf{W}}_2) \cdot \bar{\mathbf{v}} \right]. \tag{38}$$

When $\mathbf{M}$ and $\mathbf{W}$ are diagonal, the excitations in eqs (35)–(38) can be rewritten as

$$\bar{\mathbf{f}}^M = \bar{\mathbf{W}}_2 \cdot \bar{\mathbf{f}} - \bar{\mathbf{W}}_2 \cdot (\mathbf{K}_1 \cdot \bar{\sigma}) + \mathbf{K}_1 \cdot \left(\bar{\mathbf{W}}_1 \cdot \bar{\sigma} \right), \tag{39}$$

$$\dot{\bar{\mathbf{T}}}^M = \bar{\mathbf{W}}_1 \cdot \dot{\bar{\mathbf{T}}} + \bar{\mathbf{W}}_1 \cdot (\mathbf{K}_2 \cdot \bar{\mathbf{v}}) - \mathbf{K}_2 \cdot \left(\bar{\mathbf{W}}_2 \cdot \bar{\mathbf{v}} \right), \tag{40}$$

$$\bar{\mathbf{f}}^M = \bar{\mathbf{W}}_2 \cdot \bar{\mathbf{f}} + (\mathbf{I} - \bar{\mathbf{W}}_2) \cdot (\mathbf{K}_1 \cdot \bar{\sigma}) - \mathbf{K}_1 \cdot \left[(\mathbf{I} - \bar{\mathbf{W}}_1) \cdot \bar{\sigma} \right], \tag{41}$$

$$\dot{\bar{\mathbf{T}}}^M = \bar{\mathbf{W}}_1 \cdot \dot{\bar{\mathbf{T}}} - (\mathbf{I} - \bar{\mathbf{W}}_1) \cdot (\mathbf{K}_2 \cdot \bar{\mathbf{v}}) + \mathbf{K}_2 \cdot \left[(\mathbf{I} - \bar{\mathbf{W}}_2 \cdot) \bar{\mathbf{v}} \right]. \tag{42}$$

When working with the displacement-stress formulation, the corresponding mirror excitation can be obtained with the same procedure, or, by simply replacing $\dot{\bar{\mathbf{v}}}\,\bar{\mathbf{v}}$, $\dot{\bar{\sigma}}$ and $\dot{\bar{\mathbf{T}}}$ with $\ddot{\bar{\mathbf{u}}}$, $\bar{\mathbf{u}}$, $\bar{\sigma}$ and $\bar{\mathbf{T}}$ in eqs (35)–(42), respectively.

3.2 Multiple point sources method

In this section, we use the representation theorem in eq. (20) as a starting point and discretize the surface integrals to express the mirror excitation force in terms of multiple point sources. As opposed to the direct discrete differentiation method presented in Section 3.1, the present approach requires some approximations and the accuracy of the reconstructed wavefield depends on the quality of the quadrature used to discretize the surface integrals (e.g. Mittet 1994). Moreover, the surface defining the time-reversal mirror needs to be explicitly defined in the present case.

When introducing the traction density vector $\mathbf{T}$ with components $T_i = n_j C_{ijkl} \partial_k u_l$ and the moment density tensor $\mathbf{M}$ with components

$M_{kl} = u_i n_j C_{ijkl}$, eq. (20) becomes

$$u_i(\mathbf{x}) = \int_V G_{in}(\mathbf{x}, \mathbf{x}') f_n(\mathbf{x}') dV'$$

$$+ \oint_S G_{in}(\mathbf{x}, \mathbf{x}') T_n(\mathbf{x}') dS'$$

$$- \oint_S M_{kn}(\mathbf{x}') \partial_k' G_{in}(\mathbf{x}, \mathbf{x}') dS'. \tag{43}$$

The surface integrals in eq. (43) can be approximated using an arbitrary numerical quadrature having the general form

$$\int_S f(\mathbf{x}) dS \approx \sum_{i=1}^{n} \alpha_i f(\mathbf{x}_i), \tag{44}$$

where, S is the designated integration region, $f(\mathbf{x})$ is an integrand defined on V, the points $\mathbf{x}_i$ are called quadrature nodes, and α_i are the quadrature weights. As an example, in Section 5, we simply defined the surface S as a set of triangular faces in which we used a simple one-point quadrature, that is where, one quadrature node is placed at the centroid $\mathbf{x}_i$ of each face and the quadrature weight α_i is simply the area of the corresponding face. Using eq. (44), eq. (43) can be approximated with

$$u_i(\mathbf{x}) \approx \int_V G_{in}(\mathbf{x}, \mathbf{x}') f_n(\mathbf{x}') dV'$$

$$+ \sum_{i=1}^{n} \alpha_i G_{in}(\mathbf{x}, \mathbf{x}_i') T_n(\mathbf{x}_i')$$

$$- \sum_{i=1}^{n} \alpha_i M_{kn}(\mathbf{x}_i') \partial_k' G_{in}(\mathbf{x}, \mathbf{x}_i'), \tag{45}$$

where the surface integrals have been replaced by discrete sums that are easier to handle numerically. Using the Dirac delta function property $f(x) = \int_V f(x') \delta(x' - x) dx'$, the response $\mathbf{u}$ in eq. (45) can be expressed in terms of equivalent body-forces as

$$u_i(\mathbf{x}) \approx \int_V G_{in}(\mathbf{x}, \mathbf{x}') f_n(\mathbf{x}') dV'$$

$$+ \sum_{i=1}^{n} \int_V G_{in}(\mathbf{x}, \mathbf{x}_i') \alpha_i T_n \delta(\mathbf{x}' - \mathbf{x}_i) dV'$$

$$- \sum_{i=1}^{n} \int_V G_{in}(\mathbf{x}, \mathbf{x}_i') \alpha_i M_{kn} \partial_k' \delta(\mathbf{x}' - \mathbf{x}_i) dV'. \tag{46}$$

This equation does not involve the partial derivative of the Green's function anymore and has the same form as eq. (11) with the corresponding source term

$$\mathbf{f}^M = \sum_{i=1}^{n_s} \mathbf{f}_i + \sum_{i=1}^{n} \mathbf{f}_i^{\mathbf{T}} + \sum_{i=1}^{n} \mathbf{f}_i^{\mathbf{M}}, \tag{47}$$

where,

$$\mathbf{f}_i(\mathbf{x}, t) = \mathbf{s}_i(t) \delta(\mathbf{x} - \mathbf{x}_i), \tag{48}$$

$$\mathbf{f}_i^{\mathbf{T}}(\mathbf{x}, t) = \mathbf{T}_i(t) \delta(\mathbf{x} - \mathbf{x}_i) \alpha_i, \tag{49}$$

$$\mathbf{f}_i^{\mathbf{M}}(\mathbf{x}, t) = -\nabla \cdot [\mathbf{M}_i(t) \delta(\mathbf{x} - \mathbf{x}_i)] \alpha_i. \tag{50}$$

Here, we assumed that the source $\mathbf{f}$ responsible for the wavefield $\mathbf{u}$ consists of n_s single-force point sources $\mathbf{f}_i$. Provided that we are able to compute the response due to a single-force point source

and a moment tensor point source, the mirror excitation can be constructed as follow:

(i) Define explicitly the surface enclosing the volume in which we want to reconstruct the wavefield.

(ii) Approximate the surface integrals in eq. (43) using an arbitrary quadrature, that is compute the quadrature nodes $\mathbf{x}_i$, the quadrature weights α_i and the unit vectors $\mathbf{n}_i$ normal to the surface S at the quadrature nodes $\mathbf{x}_i$.

(iii) Compute and record the responses $\mathbf{u}_i$ and their derivatives due to the source $\mathbf{f}$ responsible for the original wavefield at the quadrature nodes $\mathbf{x}_i$

(iv) Evaluate the source term in eqs (48)–(50) using $T_i = n_j C_{ijkl} \partial_k u_l$ and $M_{kl} = u_i n_j C_{ijkl}$.

Imposing the time-reversal mirror then simply consists of applying all the point sources obtained simultaneously during the simulation.

3.3 Time-reversing numerical schemes

In the previous sections, we derived the mirror excitation force at any arbitrary instant. In order to reconstruct an original wavefield locally inside a subvolume surrounded by the mirror, this excitation must be applied versus time at the boundary of the subvolume.

If we wish to regenerate the original wavefield going forward in time, for a given numerical scheme, this simply consists of using the mirror excitation as the source term.

If we wish to regenerate the original wavefield going backward in time, one can adopt two different approaches.

A first approach is to use the time symmetry of the elastic wave equation. That means that one can use the same numerical scheme to regenerate the wavefield going backward as the one used to model wave propagation forward in time. In this case, the mirror excitation must be time reversed ($\mathbf{f}^M(t) \rightarrow \mathbf{f}^M(-t)$) prior to the simulation.

A second approach is to crudely undo the numerical algebra. In this case, the numerical integration scheme is modified so that the past values of the wavefield are expressed as a function of the future values of the wavefield. For example, if eq. (21) is integrated using the explicit central-difference scheme

$$\bar{\mathbf{u}}(t + \Delta t) = 2\bar{\mathbf{u}}(t) - \bar{\mathbf{u}}(t - \Delta t) + \Delta t^2 \mathbf{M}^{-1} \cdot \left[\bar{\mathbf{f}}^M(t) - \mathbf{K} \cdot \bar{\mathbf{u}}(t) \right], \tag{51}$$

to simulate the wave propagation forward in time, one can use the rearranged expression

$$\bar{\mathbf{u}}(t - \Delta t) = 2\bar{\mathbf{u}}(t) - \bar{\mathbf{u}}(t + \Delta t) + \Delta t^2 \mathbf{M}^{-1} \cdot \left[\bar{\mathbf{f}}^M(t) - \mathbf{K} \cdot \bar{\mathbf{u}}(t) \right], \tag{52}$$

to simulate the wave propagation backward in time.

When using a numerical scheme that is symmetric in time, as in our last example, both approaches are exactly equivalent. However, this is not always the case. For example, when using the second approach, an explicit scheme might transform into an implicit scheme and vice versa. Because of this, it is safer to adopt the first approach as it guarantees the stability of the simulations when going backward in time, provided that, the numerical scheme used to propagate waves forward in time is stable. The interest of the second approach lies in the fact it is potentially able to perfectly recover the original values of the wavefield if the discrete algebra is done exactly. However, rounding errors prevent such a perfect reconstruction and may lead to numerical instabilities. In our numerical examples, we preferred the first approach to time reverse the numerical scheme. The

only place where the second approach has been used is to update the memory variables needed to undo the attenuation when time-reversing a viscoelastic wavefield. This, because time reversing the attenuation is intrinsically unstable whatever the chosen approach.

3.4 Initial value

Practically, numerical simulations have a finite duration and some energy may still be present inside the subvolume where we want to reconstruct the wavefield at the time when we stop the first simulation. In order to reconstruct the wavefield perfectly using a time-reversal mirror, that energy must be accounted for as in an initial value problem in the second simulation. This can be done by taking a snapshot of the wavefield at the end of the first simulation to get the appropriate initial conditions in the time-reversed simulation. The initial conditions are obtained by applying a spatial window to the recorded wavefield, and, eventually changing the sign of the wavefield variables. When using the direct discrete differentiation method to obtain the mirror excitation, eqs (23), (33) and (34) should be used to apply the spatial window. When using the multiple point source method to compute the mirror excitation, choosing an adequate spatial window may be more delicate and depends on the number of point sources used and on the way they are implemented. One thing to keep in mind when choosing the spatial window is that the representation in eq. (43) does not match the boundary condition $\mathbf{u}^M(\mathbf{x}, t) = \mathbf{u}(\mathbf{x}, t) \, \forall \, x \in \partial M$, that is, the reconstructed wavefield is not equal to the original wavefield at the boundary of the subvolume (e.g. Fannjiang & Albert 2009). If the point sources are implemented using 1-D delta functions (e.g. Fichtner 2010) and the density of source points is large enough, a general rule of thumb is to define the Heaviside function

$$H(x) = \int_{-\infty}^{x} \delta(s) ds, \tag{53}$$

where δ is the same delta function as the one used to implement the point sources. The window function w is then obtained by inserting eq. (53) into eq. (14).

In addition to the application of the spatial window, to obtain the adequate initial conditions when invoking the time-reversal symmetry of the wave equation, the sign of odd wavefields variables (e.g. particle velocity) must be reversed while the sign of the even wavefield variables (e.g. displacement, acceleration) stays the same.

Note that the initial condition may also be obtained by running an extra simulation where the mirror is first used to reconstruct the wavefield going forward in time. At the end of this extra simulation, one can simply take a snapshot to obtain the initial conditions, applying the spatial window is not needed as the mirror has already been applied.

3.5 Attenuation

In order to regenerate the time-reversed version of an original wavefield in a visco-elastic medium, the effect of attenuation must be undone, that is, the time-reversed wavefield needs to be amplified accordingly to recover the initial amplitudes. While this amplification is straightforward to implement, it leads to numerical schemes that are intrinsically unstable as the roundoff error is amplified with the wavefield (e.g. Liu & Tromp 2006). To keep the numerical error small compared to the wavefield's amplitudes, one solution called 'checkpointing' is to periodically reset the wavefield values during the time-reversed simulation (e.g. Restrepo & Griewank 1998;

Griewank & Walther 2000; Hinze *et al.* 2005; Symes 2007). Practically that means that snapshots of the whole wavefield must be recorded periodically during the first simulation. These snapshots are then used to reset the time-reversed simulation by imposing new initial conditions as discussed in the previous section.

4 SOME PRACTICAL ASPECTS OF THE NUMERICAL IMPLEMENTATION

4.1 Finite differences

4.1.1 Acoustic equation using centred FDs

In the 2-D acoustic case, for a smoothly varying medium, and when using central FD operators to evaluate the partial derivative in eq. (3), eq. (21) takes the classic form

$$\frac{u_{i,j}^{n+1} - 2u_{i,j}^n + u_{i,j}^{n-1}}{\Delta t^2} = c^2 \left[\frac{u_{i+1,j}^n - 2u_{i,j}^n + u_{i-1,j}^n}{\Delta x^2} \right.$$
$$\left. + \frac{u_{i,j+1}^n - 2u_{i,j}^n + u_{i,j-1}^n}{\Delta y^2} \right] + f_{i,j}, \quad (54)$$

where, $u_{i,j}^n$ is the acoustic pressure at the grid node having spatial indices (i, j) and evaluated a time step (n), Δx and Δt are the spatial and time sampling intervals, respectively, and c is the sound speed. When using the centred FD scheme in eq. (54), the excitation source in eq. (24) becomes

$$f^M \big|_{i,j}^n = \frac{\tilde{u}_{i,j}^{n+1} - 2\tilde{u}_{i,j}^n + \tilde{u}_{i,j}^{n-1}}{\Delta t^2} w_{i,j}$$
$$- c^2 \left[\frac{w_{i+1,j}\tilde{u}_{i+1,j}^n - 2w_{i,j}\tilde{u}_{i,j}^n + w_{i-1,j}\tilde{u}_{i-1,j}^n}{\Delta x^2} \right.$$
$$\left. + \frac{w_{i,j+1}\tilde{u}_{i,j+1}^n - 2w_{i,j}\tilde{u}_{i,j}^n + w_{i,j-1}\tilde{u}_{i,j-1}^n}{\Delta y^2} \right]. \quad (55)$$

where $\tilde{u}$ denotes the original wavefield that we want to reconstruct locally. In Fig. 3, the grid points at which $f^M \big|_{i,j}^n$ is not equal to zero are represented by black filled squares. These points corresponds to locations at which the difference stencil (pictured in Fig. 3) overlaps the surface ∂M. We see that, in order to reconstruct the wavefield in the volume M, it is sufficient to compute and store the values f_M on a two grid point thick layer following ∂M in the present case.

Reconstructing the original wavefield $\tilde{u}$ consists in solving eq. (54) after the source term $f_{i,j}$ has been replaced with $f^M \big|_{i,j}^n$. When doing so, we notice that the values $f^M \big|_{i,j}^n$ do not need to be computed explicitly when reconstructing $\tilde{u}$. Instead, it is possible to store the displacement values $\tilde{u}$ along a two grid point thick inner layer following ∂M and to proceed as follows to update the displacement values at grid points where $f^M|_{i,j} \neq 0$

(i) Prior to evaluating the right-hand side in eq. (54), subtract the wavefield $w_{i,j}\tilde{u}_{i,j}^n$ from the current wavefield $u_{i,j}^n$ at all nodes involved in the calculation of $f^M|_{i,j}$. That is, $u_{i,j}^n \rightarrow u_{i,j}^n - \tilde{u}_{i,j}^n$ at the inner scheme nodes in Fig. 3.
(ii) Evaluate the right-hand side of eq. (54) (using the updated values $u_{i,j}^n \rightarrow u_{i,j}^n - w_{i,j}\tilde{u}_{i,j}^n$) and add the remaining term $\frac{\tilde{u}_{i,j}^{n+1} - 2\tilde{u}_{i,j}^n + \tilde{u}_{i,j}^{n-1}}{\Delta t^2} w_{i,j}$ to the result
(iii) Proceed to the time integration to obtain $u_{i,j}^{n+1}$.

From now on, we will refer to that procedure as an inner scheme as it requires to store the wavefield on an inner layer following ∂M as pictured in Fig. 3. When using eq. (25) in place of eq. (24), the
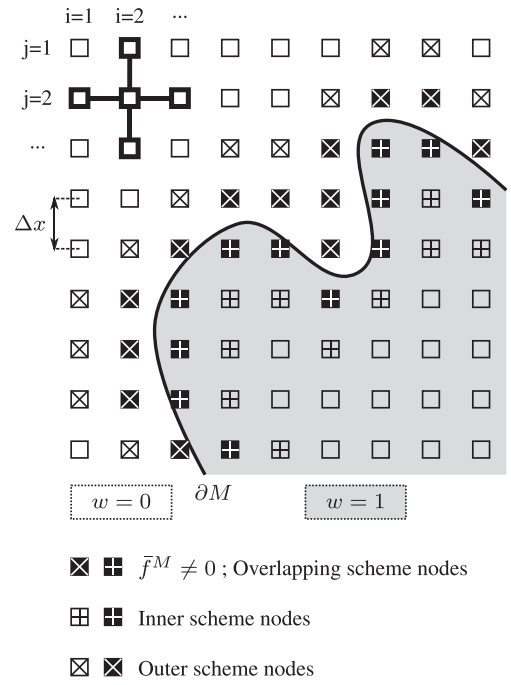

Figure 3. An example of a FD grid. The acoustic pressure is evaluated and stored at the grid nodes represented by squares. The FD stencil used to evaluate the spatial derivative is pictured in the top left corner. To regenerate a wavefield inside the grey area surrounded by ∂M, the source term in eq. (55) needs to be applied at the nodes represented by black filled squares. These are the nodes for which the FD stencil overlaps the boundary ∂M. The source term can either be computed and recorded during the first simulation or implicitly computed during the second simulation using an inner, an outer or an overlapping scheme. Depending on the chosen scheme, the acoustic pressure may be recorded at the inner scheme nodes, at the outer scheme nodes or at the overlapping scheme nodes.

mirror excitation can be expressed as

$$f^M \big|_{i,j}^n = \tilde{f}_{i,j} - \frac{\tilde{u}_{i,j}^{n+1} - 2\tilde{u}_{i,j}^n + \tilde{u}_{i,j}^{n-1}}{\Delta t^2} m_{i,j}$$
$$+ c^2 \left[\frac{m_{i+1,j}\tilde{u}_{i+1,j}^n - 2\,m_{i,j}\tilde{u}_{i,j}^n + m_{i-1,j}\tilde{u}_{i-1,j}^n}{\Delta x^2} \right.$$
$$\left. + \frac{m_{i,j+1}\tilde{u}_{i,j+1}^n - 2m_{i,j}\tilde{u}_{i,j}^n + m_{i,j-1}\tilde{u}_{i,j-1}^n}{\Delta y^2} \right], \quad (56)$$

where $m_{i,j} = (1 - w_{i,j})$. This leads to an outer scheme where the displacement values $\tilde{u}$ need to be stored along a two grid point thick outer layer following ∂M and consisting of the following steps:

(i) Prior to evaluating the right-hand side in eq. (54), add the wavefield $(1 - w_{i,j})\tilde{u}_{i,j}^n$ to the current wavefield $u_{i,j}^n$ at all nodes involved in the calculation of $f^M|_{i,j}$. That is, $u_{i,j}^n \rightarrow u_{i,j}^n + \tilde{u}_{i,j}^n$ at the outer scheme nodes in Fig. 3.
(ii) Evaluate the right-hand side of eq. (54) (using the updated values $u_{i,j}^n \rightarrow u_{i,j}^n + (1 - w_{i,j})\tilde{u}_{i,j}^n$) and add the remaining term $\tilde{f}_{i,j} - \frac{\tilde{u}_{i,j}^{n+1} - 2\tilde{u}_{i,j}^n + \tilde{u}_{i,j}^{n-1}}{\Delta t^2}(1 - w_{i,j})$ to the result.
(iii) Proceed to the time integration to obtain $u_{i,j}^{n+1}$.

It is also possible to use a mixed scheme that uses an inner scheme outside the volume M and an outer scheme inside the volume M so that the term involving the time derivative of $\tilde{u}$ vanishes. In that case, one only needs to store the values of the wavefield $\tilde{u}$ at the nodes where $f^M \neq 0$ (i.e. the black filled squares in Fig. 3). Practically, the values inside the volume M are obtained by evaluating eq. (54) after

adding the recorded values to the wavefield outside M and the values outside M are obtained by evaluating eq. (54) after subtracting the recorded values to the wavefield inside M. That last approach is certainly the easiest one to implement when using FDs and when the properties of the medium remain unchanged at the source nodes. We shall see, however, that for the FE/SEM method, using an inner or an outer scheme can greatly reduce the number of grid points at which the wavefield values must be recorded.

4.1.2 Elastic wave equation on staggered grids

The FD method on staggered grids was first introduced to model electromagnetic wave propagation (Yee 1966) and was later adapted to model elastic-wave propagation (e.g. Virieux 1986). Most staggered FD numerical schemes are based on the velocity-stress formulation where eqs (31) and (32) are time integrated using the leapfrog scheme

$$\bar{\mathbf{v}}(t + \Delta t/2) = \bar{\mathbf{v}}(t - \Delta t/2) + \Delta t \mathbf{M}^{-1} \cdot \left[\bar{\mathbf{f}}(t) - \mathbf{K}_1 \cdot \bar{\sigma}(t) \right],$$
(57)

$$\bar{\sigma}(t + \Delta t) = \bar{\sigma}(t - \Delta t) + \Delta t \left[\dot{\bar{\mathbf{T}}}(t + \Delta t/2) + \mathbf{K}_2 \cdot \bar{\mathbf{v}}(t + \Delta t/2) \right].$$
(58)

Knowing the stress field $\bar{\sigma}$ at time (t), eq. (57) is used first to update the velocity field $\bar{\mathbf{v}}$ from time (t) to time ($t + \Delta t/2$). Then, knowing the velocity field $\bar{\mathbf{v}}$ at time ($t + \Delta t/2$), eq. (58) is used to update the stress field $\bar{\mathbf{v}}$ from time (t) to time ($t + \Delta t$). The matrices $\mathbf{K}_1$ and $\mathbf{K}_2$ are obtained by FD approximations of the spatial derivatives in the wave equation. For example, when using a fourth-order approximation (e.g. Levander 1988), the derivative of the stress field $\bar{\sigma}_{xx}$ with respect to x is approximated by

$$\frac{\partial \bar{\sigma}_{xx}}{\partial x}\bigg|_{i,j,k}^n \approx -\frac{1}{24\Delta x} \left[\bar{\sigma}_{xx}|_{i+\frac{3}{2},j,k}^n - \bar{\sigma}_{xx}|_{i-\frac{3}{2},j,k}^n \right]$$
$$+ \frac{9}{8\Delta x} \left[\bar{\sigma}_{xx}|_{i+\frac{1}{2},j,k}^n - \bar{\sigma}_{xx}|_{i-\frac{1}{2},j,k}^n \right],$$
(59)

where i, j, k are the spatial indices, and n is the time step index. In order to implement the time-reversal mirror, one simply needs to substitute the source terms $\bar{\mathbf{f}}$ and $\dot{\bar{\mathbf{T}}}$ in eqs (57) and (58) with the mirror excitations in eqs (39)–(42). As shown in Fig. 4, because the fourth-order FD operator expands over four grid nodes, the excitations $\bar{\mathbf{f}}^M$ and $\dot{\bar{\mathbf{T}}}^M$ are imposed on a three grid point thick layer following the surface of the subvolume where we want to regenerate the wavefield. As for the acoustic scheme, it is also possible to impose the mirror excitation using an inner, an outer or an overlapping scheme. These schemes can be obtained by the procedure described in the previous section applied to eqs (57) and (58), independently. In this case, the velocity field $\bar{\mathbf{v}}$ and the stress field $\bar{\sigma}$ must be recorded on a three grid point layer thick inside, outside or overlapping the boundary ∂M, depending on the chosen scheme, as pictured in Fig. 4. In fact, implementing the time-reversal mirror using an overlapping scheme combined with the fourth-order space accurate FD scheme introduced by Levander (1988) is exactly equivalent to the 'wave-injection' method proposed by Robertsson & Chapman (2000).

4.2 Spectral element

The SEM method was first introduced to solve fluid dynamics problems (e.g. Patera 1984; Maday & Patera 1989) and later adapted to
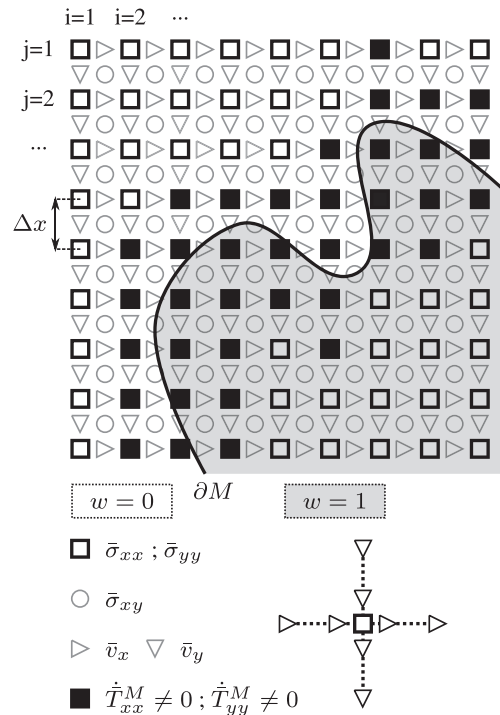

Figure 4. An example of a 2-D staggered FD grid as introduced by Virieux (1986) to model the propagation of elastic waves. The FD stencil used to evaluate the spatial derivative at the nodes represented by squares is pictured in the bottom right corner. The black squares shows the nodes at which the normal component $\dot{\bar{T}}_{xx}^M$ and $\dot{\bar{T}}_{yy}^M$ of the tensor $\dot{\bar{\mathbf{T}}}^M$ in eqs (35)–(42) have a non-zero value. These are the nodes where the FD stencil overlaps the boundary ∂M. The nodes where the remaining source terms $\dot{\bar{T}}_{xy}^M$, $\bar{f}_x^M$ and $\bar{f}_y^M$ take a non-zero value can be obtained similarly by checking whether or not the FD stencil overlaps the boundary ∂M. As in the acoustic case, these source terms can either be computed and recorded during the first simulation or implicitly computed during the second simulation using an inner, an outer, or an overlapping scheme. As the FD stencil extends over four grid points, all the fields need to be recorded on a three grid point thick layer inside, outside or overlapping the boundary ∂M, when using an inner, an outer or an overlapping scheme, respectively.

simulate wave propagation (Seriani *et al.* 1995; Faccioli *et al.* 1997; Komatitsch 1997). In this method, the computational domain is divided into elements where the solution of the problem is expressed in terms of local basis functions compactly supported inside the elements. For example, the discrete approximation of the p-component $\bar{u}_p$ of the displacement vector inside the element G_e is expressed as:

$$\bar{u}_p(\mathbf{x}, t)\big|_{\mathbf{x} \in G_e} = \sum_{i=1}^{N_\psi} u_p\big|_e^i(t) \psi_e^i(\mathbf{x}),$$
(60)

where, ψ_e^i is the ith basis function inside element G_e and $u_p\big|_e^i(t)$ are the corresponding expansion coefficients. When taking the Galerkin projection of the wave equation, for each element G_e, one obtains the local, that is element-wise discrete force balance

$$\mathbf{M}_e \cdot \ddot{\mathbf{u}}_e(t) + \mathbf{K}_e \cdot \mathbf{u}_e(t) = \mathbf{f}_e(t), \quad e = 1, \ldots, n_e,$$
(61)

where $\mathbf{u}_e$, $\mathbf{M}_e$ and $\mathbf{K}_e$ are the local coefficient vector, the local mass matrix and the local stiffness matrix, respectively. The local linear systems in eq. (61) can then be assembled to obtain the global force balance

$$\mathbf{M}_{\text{global}} \cdot \ddot{\mathbf{u}}_{\text{global}}(t) + \mathbf{K}_{\text{global}} \cdot \mathbf{u}_{\text{global}}(t) = \mathbf{f}_{\text{global}}(t),$$
(62)

where $\mathbf{u}_{\text{global}}$, $\mathbf{M}_{\text{global}}$ and $\mathbf{K}_{\text{global}}$ are the global versions of the coefficient vector, the mass matrix and the stiffness matrix, respectively. We refer to the excellent book by Fichtner (2010), for practical details on obtaining eq. (61) and assembling the linear system in eq. (62). Some useful information can also be found in Pozrikidis (2005) and Hughes (1987).

In order to implement the time-reversal mirror using the SEM method, it is natural to define a local mirror excitation vector $\mathbf{f}_e^M$ in each element as

$$\mathbf{f}_e^M = \mathbf{M}_e \cdot \ddot{\mathbf{u}}_e^M + \mathbf{K}_e \cdot \mathbf{u}_e^M, \tag{63}$$

where the vector $\mathbf{u}_e^M$ contains the expansion coefficients corresponding to the discrete approximation $\bar{\mathbf{u}}_e^M$ inside element G_e of the windowed wavefield $\mathbf{u}^M$ defined in eq. (6). The linear systems in eq. (63) can then be assembled to obtain the global mirror excitation

$$\mathbf{f}_{\text{global}}^M = \mathbf{M}_{\text{global}} \cdot \ddot{\mathbf{u}}_{\text{global}}^M + \mathbf{K}_{\text{global}} \cdot \mathbf{u}_{\text{global}}^M. \tag{64}$$

In the SEM method, the basis functions ψ_e^i are usually Lagrange polynomials of degree $(N_\psi - 1)$ constructed using the Gauss-Lobatto-Legendre (GLL) collocation points. In that case, the discrete approximation of the p-component $\bar{u}_p^M$ of the displacement vector $\mathbf{u}_e^M$ can be expressed as

$$\bar{u}_p^M(\mathbf{x}, t)\big|_{\mathbf{x} \in G_e} = \sum_{i=1}^{N_\psi} u_p^M\big|_e^i(t)\psi_e^i(\mathbf{x}) \tag{65}$$

$$= \sum_{i=1}^{N_\psi} w_e^i \, u_p\big|_e^i(t)\psi_e^i(\mathbf{x}), \tag{66}$$

where $u_p\big|_e^i(t)$ are the expansion coefficients associated with the original wavefield that we want to regenerate inside the mirror, and the coefficient w_e^i simply correspond to the values of the window function $w(\mathbf{x})$ evaluated at the GLL points. By identifying the terms on the right-hand side of eq. (66) we obtain

$$\mathbf{u}_e^M = \mathbf{W}_e \cdot \mathbf{u}_e, \tag{67}$$

where $\mathbf{W}_e$ is the diagonal matrix

$$\mathbf{W}_e = \begin{bmatrix} w_e^1 & \cdots & 0 \\ \vdots & \ddots & \vdots \\ 0 & \cdots & w_e^{N_\psi} \end{bmatrix}. \tag{68}$$

One big advantage of the SEM method is that the mass matrices $\mathbf{M}_e$ are diagonal. In this case, inserting eq. (67) into eq. (63) and using eq. (61), the mirror excitation can be expressed as

$$\mathbf{f}_e^M = \mathbf{W}_e \cdot \mathbf{f}_e - \mathbf{W}_e \cdot (\mathbf{K}_e \cdot \mathbf{u}_e) + \mathbf{K}_e \cdot (\mathbf{W}_e \cdot \mathbf{u}_e), \tag{69}$$

or equivalently, when subtracting eq. (61) to eq. (69),

$$\mathbf{f}_e^M = \mathbf{W}_e \cdot \mathbf{f}_e + (\mathbf{I} - \mathbf{W}_e) \cdot (\mathbf{K}_e \cdot \mathbf{u}_e) - \mathbf{K}_e \cdot [(\mathbf{I} - \mathbf{W}_e) \cdot \mathbf{u}_e]. \tag{70}$$

When ignoring the source term $\mathbf{W}_e \cdot \mathbf{f}_e$, the mirror excitation as expressed in eq. (69) is simply the difference between the local internal force calculated using the windowed wavefield and the windowed version of the internal force calculated from the full wavefield (i.e. not windowed). Eq. (70) is similar but the window function w is replaced by the negative of the complementary window function $(1 - w)$.

When inserting $\mathbf{W}_e = \alpha_e \mathbf{I}$, where, α_e is a scalar coefficient, and $\mathbf{I}$ is the identity matrix, in eqs (69) and (70), we see that $\mathbf{f}_e^M$ is effectively zero inside the element G_e. That means that, the only

$w = 0$ ∂M $w = 1$

◆ Inner scheme nodes   ◇◆ $\mathbf{f}_e^M \neq 0$
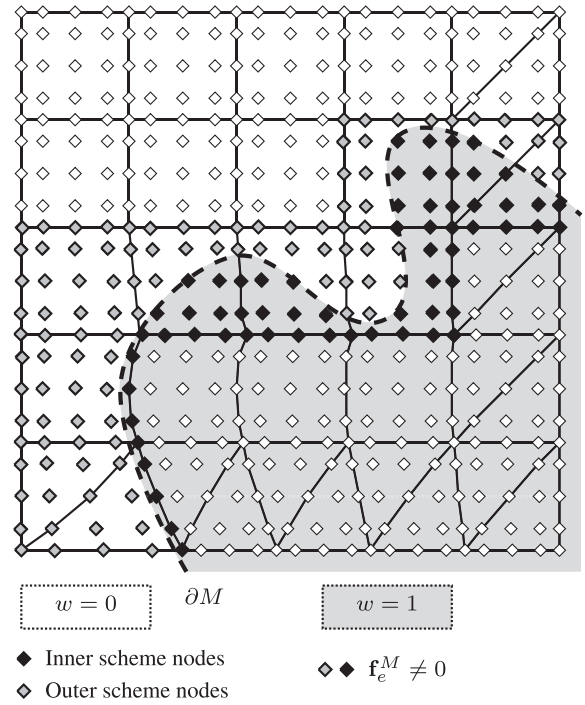◇ Outer scheme nodes

Figure 5. An example of a 2-D FE/SEM grid containing quadrilateral and triangular elements, delimited by solid lines. The diamond symbols represents the grid nodes at where the wavefield values are evaluated. The black filled diamonds shows the grid nodes at which the wavefield values needs to be known to compute the mirror excitation when using an inner scheme. The grey filled diamonds shows the grid nodes at which the wavefield values needs to be known to compute the mirror excitation when using an outer scheme.

elements that contribute to the mirror excitation $\mathbf{f}_{\text{global}}^M$ are the ones where the value of the window function w evaluated at the GLL nodes is not constant. In other words, these are the elements crossed by the surface ∂M bounding the subvolume in which we wish to regenerate the wavefield.

To implement the mirror, the local excitations $\mathbf{f}_e^M$ may be calculated during a first simulation and stored. Then, in a second simulation, the mirror is applied by inserting the stored values as the source term in eq. (61) prior to the assembly of the global system. However, this approach requires to store the local mirror excitations at all GLL points inside each element contributing to the global mirror excitation. We now show that, as with the FD method, it is also possible and preferable to store the wavefield values instead of the excitations themselves. Consider the case where the window function w used to construct the mirror is equal to one inside the subvolume M bounded by ∂M and zero outside, as pictured in Fig. 5. On the one hand, in order to evaluate the mirror excitation in one element G_e using eq. (69), we need to know both the internal force $\mathbf{f}_e^{\text{int}} = (\mathbf{K}_e \cdot \mathbf{u}_e)$ and the displacement $\mathbf{u}_e$ at the GLL nodes inside the subvolume M. On the other hand, in order to evaluate the mirror excitation using eq. (70), we need to know both the internal force $(\mathbf{K}_e \cdot \mathbf{u}_e)$ and the displacement $\mathbf{u}_e$ at the GLL nodes outside the subvolume M. In the worst case, the surface ∂M splits the GLL nodes in two equal halves and using either one of eqs (69) and (70) requires the same amount of disk space to store the values of $\mathbf{f}_e^{\text{int}}$ and $\mathbf{u}_e$ at the GLL nodes involved in the calculation of $\mathbf{f}_e^M$. In the best case, the surface ∂M follows the boundary of the element and one only needs to store the values of $\mathbf{f}_e^{\text{int}}$ and $\mathbf{u}_e$ at some GLL nodes on the faces of the element, as pictured in Fig. 5. Hence, for minimizing the disk

usage, we propose to adopt the following procedure to implement numerical mirrors using the SEM method:

(i) Select all elements where the window function evaluated at the GLL nodes is not constant (e.g. the elements crossed by the surface ∂M when using a binary window function w).

(ii) For all the selected elements, check which of the window function w and the complementary window function $(1 - w)$ is equal to zero at most GLL nodes.

(iii) In the situation where $w = 0$ at most GLL nodes, record the local internal force and the displacement at the GLL nodes where $w \neq 0$ during the first simulation. Then, impose the mirror using eq. (69) in the second simulation.

(iv) In the situation where $(1 - w) = 0$ at most GLL nodes, record the local internal force and the displacement at the GLL nodes where $(1 - w) \neq 0$ during the first simulation. Then, impose the mirror using eq. (70) in the second simulation.

Practically, implementing the mirror using the SEM method simply consists of modifying the way the local internal forces are computed in the elements where $\mathbf{f}_e^M \neq 0$. When using eq. (69) to compute the mirror excitation, the local internal forces can be obtained using the following inner scheme procedure:

(i) Prior to the computation of the internal forces in each element, add the recorded value of the displacement to the current value of the displacement.
(ii) Compute the local internal force in the elements.
(iii) Subtract the recorded values of the local internal force from the value of the local internal force computed in the previous step.

When using eq. (70) to compute the mirror excitation, the local internal forces can be obtained using the following outer scheme procedure:

(i) Prior to the computation of the internal forces in each element, subtract the recorded value from the displacement to the current value of the displacement,
(ii) Compute the local internal force in the elements,
(iii) Add the recorded values of the local internal force to the value of the local internal force computed in the previous step.

5 NUMERICAL EXAMPLES AND APPLICATIONS

5.1 A simple time-reversal mirror

We first illustrate the different source terms in eqs (1), (2) and (43) that are needed to regenerate a time-reversed wavefield. In Fig. 7, we present forward and time-reversed simulations where a spherical P wave is propagating through a homogeneous medium. We used a FD method (Levander 1988) to model wave propagation in an elastic medium. The grid used in the simulation has dimensions $175\Delta x \times 175\Delta y \times 175\Delta z$, where, $\Delta x = \Delta y = \Delta z = 2/3$ m. The represented grid chunk in the figure has dimensions: $115\Delta x \times 115\Delta y \times 115\Delta z$. The P-wave velocity of the propagating medium is $V_p = 2152$ m s^{-1}, the S-wave velocity is $V_s = 1310$ m s^{-1} and the density is $\rho = 2650$ kg m^{-3}. The total duration of the simulation is $300\Delta t$, where, $\Delta t = 1.327 \times 10^{-4}$ s. We used an explosive source placed at the centre of the grid with a Gaussian source time function that is producing a pulse with central frequency $f_c = 225$ Hz. The different snapshots are taken at times $t_1 = 0$, $t_2 = 60\Delta t$, $t_3 = 120\Delta t$, $t_4 = 180\Delta t$.
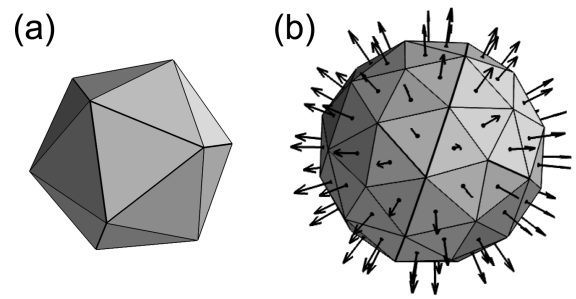

Figure 6. (a) An icosahedron. (b) An *icosphere* obtained by successive subdivision of the original icosahedron. The time-reversal mirror is constructed by placing a point source at the barycentre of each triangular face of the *icosphere*. The amplitude of the point sources is proportional to the area of the faces. The arrows represent the vectors normal to the faces.

In the time-reversed simulations, we implemented the time-reversal mirror using the multiple point source method described in Section 3.2. We constructed a spherical mirror by successive subdivision of an icosahedron as presented in Fig. 6. The radius of the ico-sphere is $r = 23.3$ m. We used three subdivision steps that result in a total number of point sources $N_{src} = 2 \times 1280 + 1$. That is: One sink point source, that is the first term on the right-hand side in eqs (2), (43) and (47) that is the time reversed-version of the source responsible for the original wavefield; 1280 monopole sources, that is the second terms on the right-hand side in eqs (2), (43) and (47) involving the Green's function; 1280 dipole sources, that is the third terms on the right-hand side in eqs (2), (43) and (47) involving the derivative of the Green's function.

Fig. 7(a) shows the forward simulation where the P wave is expanding versus time around the point source. The simulation starts at time $t = 0$ and ends at time $t = 300\Delta t$.

Fig. 7(b) shows the backward simulation where the time-reversal mirror is used to regenerate the time-reversed wavefield. The simulation starts at time $t = 300\Delta t$ and ends at time $t = 0$. In this simulation, all the source terms in eqs (2), (43) and (47) are implemented.

Fig. 7(c) shows a backward simulation where only the monopole sources are accounted for. We see that, these sources generate a two way wavefield, that is one P wave going inward the mirror, and one P wave going outward the mirror. As we are looking at the bulk-pressure, these two waves have opposite polarities. Note that the amplitude of these two waves is half the one of the original P wave represented in Fig. 7(a) when comparing identical positions of the waves.

Fig. 7(d) shows a backward simulation where only the dipole sources are accounted for. As with the monopoles sources, we observe a two way wavefield. The difference is that, in this case, these two waves have similar polarities. As for the monopole sources, the amplitude of these two waves is half that of the original P wave.

Fig. 7(e) shows a backward simulation where both the monopoles and the dipole sources have been accounted for. As the two wavefields, generated by the monopole and the dipole sources, have opposite polarities outside the mirror, the outgoing waves cancel out. The resulting wavefield is a one-way wavefield emitted inward the mirror. Inside the mirror, the two wavefields are in phase and their amplitudes add up to match that of the original wavefield in Fig. 7(a). As we are going backward in time, the spherical wave produced is refocusing in time and space at the source location. However, we observed that, after it has refocused, the spherical wave is expanding again as time is going backward. To cancel out
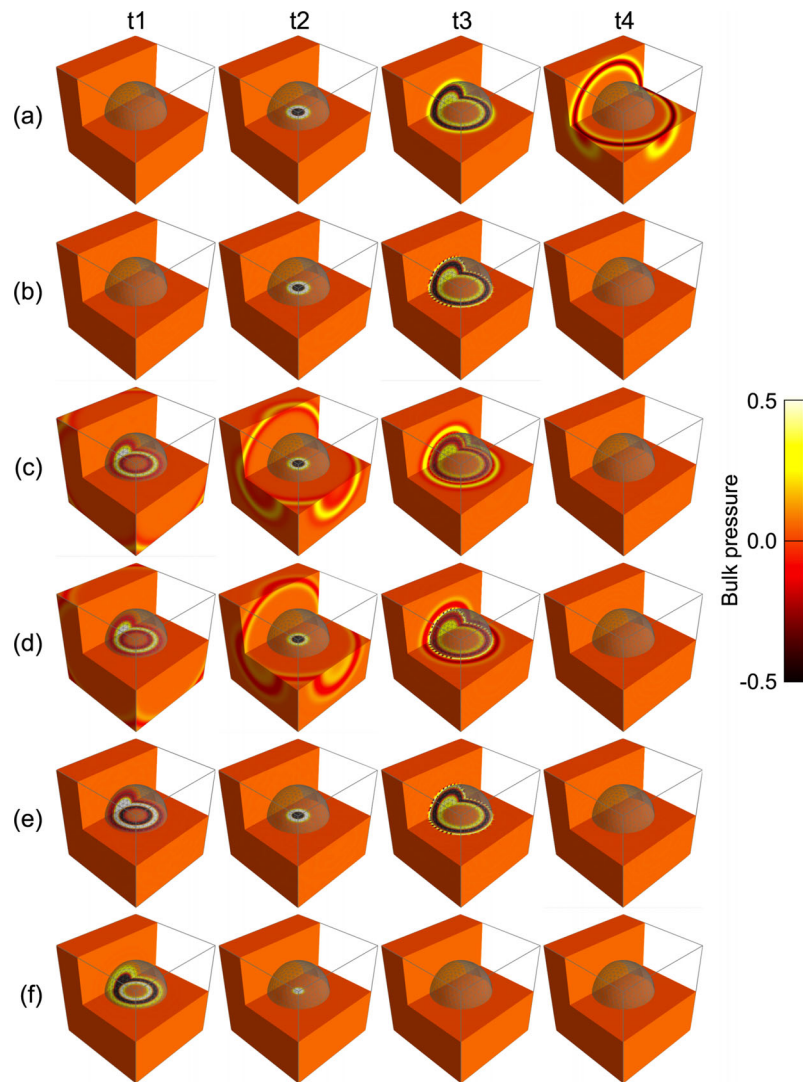
Figure 7. Snapshots showing the Bulk pressure (i.e. $\sigma_{xx} + \sigma_{yy} + \sigma_{zz}$) at four different instants in the forward simulation (a) and in various time-reversed simulations (b, c, d, e, f). The transparent sphere represents the time-reversal mirror. The grid used in the simulation has dimensions $175\Delta x \times 175\Delta y \times 175\Delta z$, where, $\Delta x = \Delta y = \Delta z = 2/3$ m. The represented grid chunk in the figure has dimensions: $115\Delta x \times 115\Delta y \times 115\Delta z$. The *P*-wave velocity of the propagating medium is $V_p = 2152$ m s^{-1}, the *S*-wave velocity is $V_s = 1310$ m s^{-1} and the density is $\rho = 2650$ kg m^{-3}. The total duration of the simulation is $300\Delta t$, where, $\Delta t = 1.327 \times 10^{-4}$ s. We used an explosive source placed at the centre of the grid with a Gaussian source time function that is producing a pulse with central frequency $f_c = 225$ Hz. The different snapshots are taken at times $t_1 = 0$, $t_2 = 60\Delta t$, $t_3 = 120\Delta t$, $t_4 = 180\Delta t$. The different time-reversed simulations illustrate the wavefields generated by the monopole, the dipole and the sink components of the mirror's excitation. (a) Forward simulation. (b) Complete time-reversed simulation where all the source terms are accounted for, that is, the monopole sources, the dipole sources and the sink. (c) Time-reversed simulation where only the monopole sources are accounted for. (d) Time-reversed simulation where only the dipole sources are accounted for. (e) Time-reversed simulation where both the monopole and the dipole sources are accounted for. (f) Time-reversed simulation where only the sink is accounted for.

this spherical wave propagating at negative times, one must add the sink term represented in Fig. 7(f). We then obtain the desired time-reversed wavefield plotted in Fig. 7(b).

Fig. 7(f) shows a backward simulation where only the sink source is accounted for. It generates a one way wavefield expanding around the source. It produces the same wavefield as in Fig. 7(a) but the wave front is expanding as time is going backward.

5.2 Using a time-reversal mirror to regenerate a wavefield going forward in time

Fig. 8 illustrates the fact that the time-reversal mirror tool can also be used to regenerate an original wavefield going forward with respect to time.

Fig. 8(a) is similar to Fig. 7(a) and pictures the wavefield observed in the forward simulation.

The wavefield pictured in Fig. 8(b) looks similar to the one in Fig. 7(b) but has been regenerated going forward in time. Interestingly, in that case, the mirror acts as a perfect absorbing boundary.

The simulations presented in Figs 8(c)–(f) are similar to those in Figs 7(c)–(f), respectively, but the source time functions associated with the monopole sources, the dipole sources and the sink source have not been time reversed.

The wavefields presented in Figs 8(c) and (d) are generated by the monopole sources an the dipole sources, respectively. Outside the mirror they have the same polarity, opposite to the one of the original wavefield in Fig. 8(a). Inside the mirror, they have opposite polarities. Both wavefields have the same absolute amplitudes.
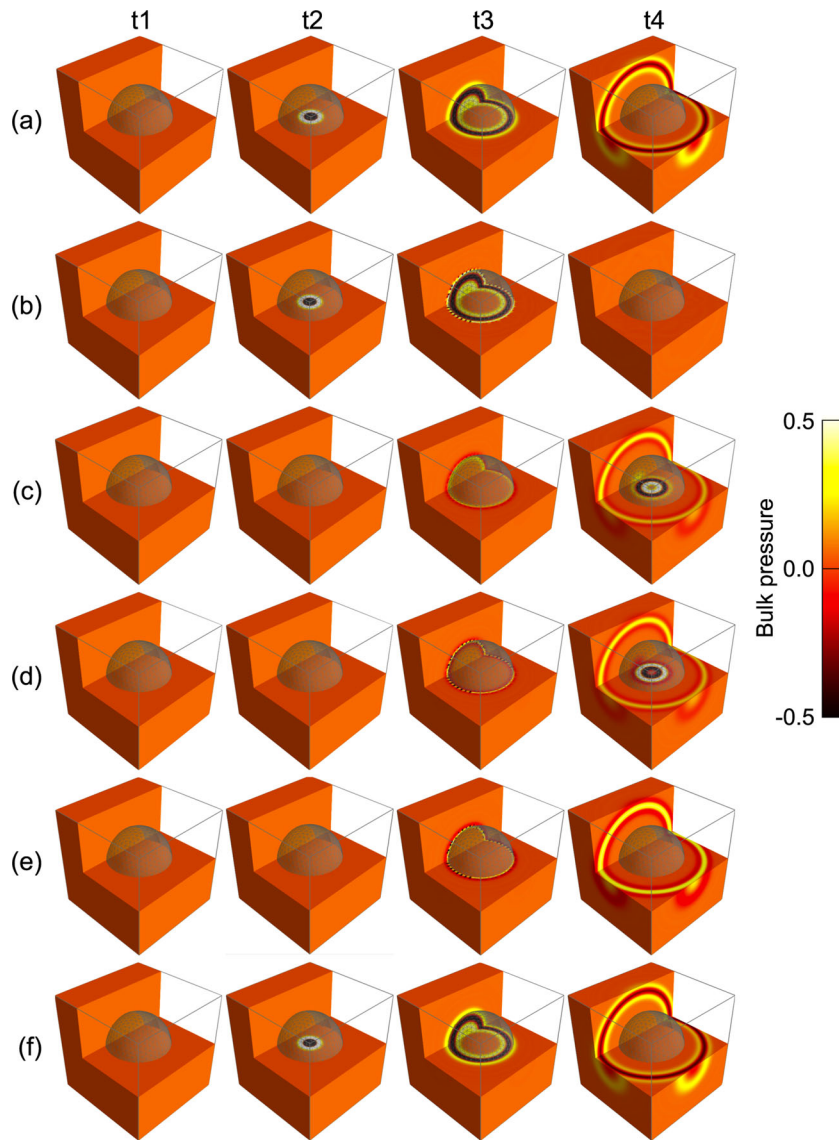
Figure 8. Snapshots showing the Bulk pressure (i.e. $\sigma_{xx} + \sigma_{yy} + \sigma_{zz}$) at four different instants in various forward simulations. The transparent sphere represents the time-reversal mirror. The grid used in the simulation has dimensions $175\Delta x \times 175\Delta y \times 175\Delta z$, where, $\Delta x = \Delta y = \Delta z = 2/3$ m. The represented grid chunk in the figure has dimensions: $115\Delta x \times 115\Delta y \times 115\Delta z$. The *P*-wave velocity of the propagating medium is $V_p = 2152$ m s^{-1}, the *S*-wave velocity is $V_s = 1310$ m s^{-1} and the density is $\rho = 2650$ kg m^{-3}. The total duration of the simulation is $300\Delta t$, where $\Delta t = 1.327 \times 10^{-4}$ s. We used an explosive source placed at the centre of the grid with a Gaussian source time function that is producing a pulse with central frequency $f_c = 225$ Hz. The different snapshots are taken at times $t_1 = 0$, $t_2 = 60\Delta t$, $t_3 = 120\Delta t$, $t_4 = 180\Delta t$. The different simulations are comparable to the one in Fig. 7 but are not time reversed. (a) Forward simulation, that is with no mirror. (b) Forward simulation with the mirror and where all the source terms are accounted for, that is, the monopole sources, the dipole sources and the sink. (c) Forward simulation where only the monopole source component of the mirror are accounted for. (d) Forward simulation where only the dipole source component of the mirror are accounted for. (e) Forward simulation where both the monopole and the dipole source components of the mirror are accounted for. (f) Forward simulation whith the time-reversed sink only.

In Fig. 8(e), we see that the wavefield generated by the monopole sources and the dipole sources taken together is a one way wavefield going outward from the mirror. This is because the two wavefields interfere destructively and constructively inside and outside the mirror, respectively. This wavefield has the same amplitude as the one in Fig. 8(a) but has an opposite sign. Hence, it cancels out the original wavefield as it escapes the mirror.

When regenerating a wavefield going forward in time, the sink term is just the source itself and simply regenerates the original wavefield as pictured in Fig. 8(f).

5.3 Using the direct discrete differentiation method to construct time-reversal mirrors having complex geometry

In Fig. 9, we emphasize the fact that the direct discrete differentiation method permits to implement time-reversal mirrors having complicated geometry with ease. We used 2-D centred FDs to solve the acoustic wave equation as discussed in Section 4.1.1. In the forward simulation, we propagated a plane wave into a random medium obtained by smoothing a spatial realization of the white noise. The spatial distribution of the sound speed in the medium is pictured in the left-hand panel of Fig. 9(a). The plane wave has been
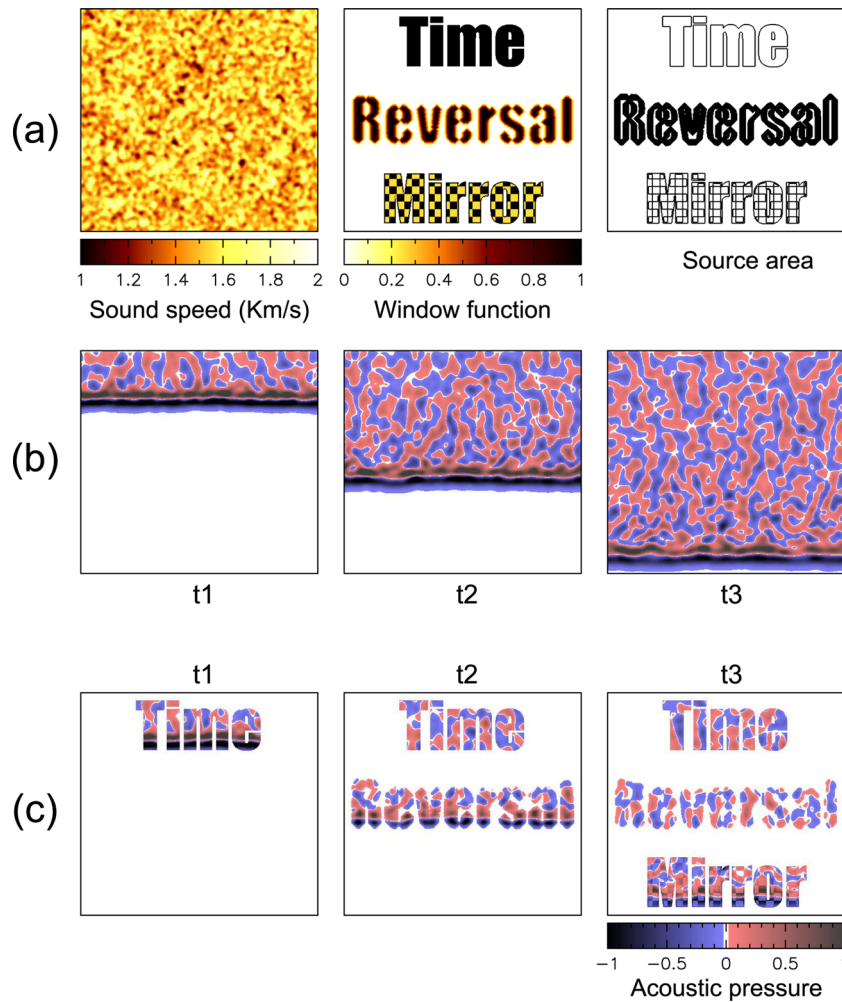
Figure 9. (a) From left to right, fluctuation of the sound speed in the propagating medium, window function $w(x, y)$ implicitly defining the time-reversal mirror, source area (i.e. grid points where the right-hand side of eqs (55) and (56) is not equal to zero). (b) Snapshot showing a plane wave propagating through the medium at three different instants ($t_1 = 414\Delta t$, $t_2 = 828\Delta t$, $t_3 = 1242\Delta t$). The model has dimensions $469\Delta x \times 441\Delta y$, where $\Delta x = \Delta y = 1$ m. The total duration of the simulation is $1300\Delta t$, where, $\Delta t = 2.5 \times 10^{-4}$ s. (c) Snapshot showing the wavefield in (b) regenerated locally using the time-reversal mirror.

injected by forcing the acoustic pressure to match a time-varying boundary condition at the top side of the domain. The source pulse is the derivative of a Gaussian with central frequency $f_c = 32$ Hz. In the horizontal direction, we applied periodic boundary conditions to simulate an infinite medium. The model has dimensions $469\Delta x \times 441\Delta y$, where $\Delta x = \Delta y = 1$ m. The total duration of the simulation is $1300\Delta t$, where, $\Delta t = 2.5 \times 10^{-4}$s.

In Fig. 9(b), we present three snapshots taken during the forward simulation at time $t_1 = 414\Delta t$, $t_2 = 828\Delta t$, $t_3 = 1242\Delta t$. We observe that the fluctuation of the sound speed in the propagating medium induces a significant amount of scattering that results in a complicated wavefield.

To construct the time-reversal mirror excitation, we first constructed the spatial window function w pictured in the central panel of Fig. 9(a). The function w has value one inside the 'Time' word and zero outside. For the 'Reversal' word, we smoothed the edges of the letters so the function w goes gradually from zero to one. Inside the 'Mirror' word, we used a checkerboard pattern where the values of the function w alternate between $1/4$ and 1.

During the forward simulation, we directly evaluated the right-hand side of eq. (55) and stored the value of f^M at the desired grid nodes, that is the nodes where $f^M \neq 0$. These nodes are pictured

in black on the right-hand side of Fig. 9(a). At the end of the simulation, we took a snapshot of the acoustic pressure, which was then multiplied by the spatial window w to obtain the initial condition needed in the time-reversed simulation.

In the time reversed simulation, the stored values of f^M were used as the source term. The wavefield regenerated by the time-reversal mirror is pictured in Fig. 9(c). At any given point the value of the regenerated wavefield is exactly equal to the value of the original wavefield in Fig. 9(b) multiplied by the window function in the central panel of Fig. 9(a). The error in the regenerated wavefield is virtually zero as it is entirely due to round-off errors that are also present in the forward wavefield.

5.4 Comparison between the direct discrete differentiation method and the multiple point sources method

In Fig. 10, we compare results obtained with the direct discrete differentiation method to results obtained with the multiple point sources method and when using a similar setup. We used a FD method (Levander 1988) to model wave propagation in an elastic medium. The numerical grid has dimensions: $150\Delta x \times 150\Delta y \times 150\Delta z$, where $\Delta x = \Delta y = \Delta z = 2/3$ m. The
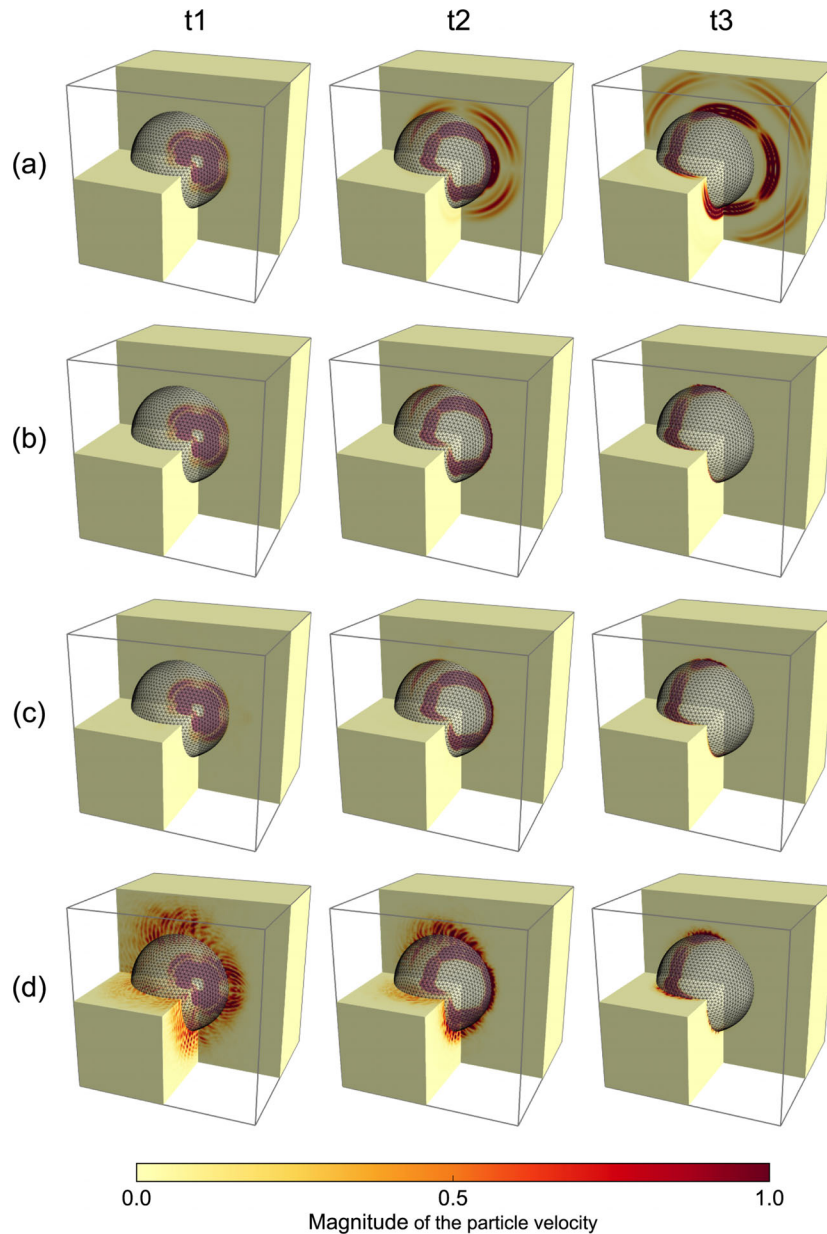
Figure 10. Comparison of the regenerated wavefields when using the direct discrete differentiation method and the multiple point source method. The snapshots shows the particle velocity at three different instants. The numerical grid has dimensions: $150\Delta x \times 150\Delta y \times 150\Delta z$, where, $\Delta x = \Delta y = \Delta z = 2/3$ m. The duration of the simulations is duration of the simulation $250\Delta t$, where, $\Delta t = 1.327 \times 10^{-4}$ s. The S-wave velocity is $V_s = 1310$ m s^{-1}, the P-wave velocity is $V_p = 2152$ m s^{-1} and the density is $\rho = 2650$ kg m^{-3}. We used a double couple source, located at the centre of the domain. The mirror has a spherical shape with radius $r_s = 28.57$ m and its centre has coordinates $x_s = 49.3$, $y_s = 39.8$ and $z_s = 49.3$. (a) Forward simulation. (b) Time-reversed simulation where the time-reversal mirror is implemented using the direct discrete differentiation method. (c) Time-reversed simulation where the time-reversal mirror is implemented using the multiple point sources method. (d) Same as in (c) but the number of point sources used has been reduced by a factor four.

duration of the simulations is duration of the simulation $250\Delta t$, where $\Delta t = 1.327 \times 10^{-4}$ s. The S-wave velocity is $V_s = 1310$ m s^{-1}, the P-wave velocity is $V_p = 2152$ m s^{-1} and the density is $\rho = 2650$ kg m^{-3}. We used a double couple source, located at the centre of the domain, with moment tensor

$$\mathbf{M}_0 = \begin{vmatrix} 0 & 0 & 0 \\ 0 & 0 & 1 \\ 0 & 1 & 0 \end{vmatrix}. \tag{71}$$

The mirror has a spherical shape with radius $r_s = 28.57$ m. The centre of the sphere has coordinates $x_s = 49.3$, $y_s = 39.8$ and

$z_s = 49.3$. We intently offset the centre of the mirror with respect to the source position so that the different wavefronts are not parallel to the mirror. In addition we stopped the forward simulation at a time when some wave energy is still present inside the mirror so that initial conditions must be imposed in the time-reversed simulations.

The wavefield observed in the forward simulation is pictured in Fig. 10(a). In Fig. 10(b), we present the result of a time reversed simulation where the mirror was implemented using the direct discrete differentiation method. The mirror was defined using a window function w that takes the value one at nodes inside the sphere and the value zero at nodes outside the sphere. To obtain the necessary initial conditions, we simply took a snapshot of the wavefield at

the end of the forward simulation and multiplied it by the window function. The wavefield presented has been obtained using the inner scheme procedure described in Section 4.1.2 to implement the mirror. The other schemes give similar results that are not presented. As we already discussed, the error in the regenerated wavefield is virtually inexistent as it is entirely due to round-off errors that are also affecting the forward wavefield.

In Fig. 10(c), we present the result of a time-reversed simulation where the mirror was implemented using the multiple point source method. We constructed the mirror by successive subdivision of an icosahedron as presented in Fig. 6. We used four subdivision steps that result in a total number of point sources $N_{src} = 2 \times 5120 + 1$. This corresponds to an average distance $d = 1.02\Delta x$ between two neighbouring point sources. It corresponds to eight points per wavelength for the S wave that is roughly the minimum number of points per wavelength required to accurately model the propagation of S waves. To construct the initial conditions, we defined the window function

$$w = \begin{vmatrix} 0 & \forall & & \phi & < -l \\ \frac{1}{2}\left[1 + \sin\left(\frac{\pi\phi}{2l}\right)\right] & \forall & -l < & \phi & < l \\ 1 & \forall & l < & \phi & \end{vmatrix}, \quad (72)$$

where

$$\phi(x, y, z) = r_s - \sqrt{(x - x_s)^2 + (y - y_s)^2 + (z - z_s)^2} \quad (73)$$

is the signed distance function, and l is the thickness of a layer in which the window function is gradually varying form zero to one. The initial conditions are obtained by taking a snapshot at the end

of the forward simulation, changing the sign of the velocity and multiplying the stress and the velocity by the window function in eq. (72). Note that the window function w is effectively taking the value $1/2$ on the mirror's surface so the initial conditions match the boundary conditions in eq. (2). In this example, we observe that, when using a sufficient number of point source per wavelength, the error in the regenerated wavefield is barely visible and not problematic.

Fig. 10(d) has been obtained in the same way as Fig. 10(c) but the number of point sources has been divided by four, that is $N_{src} = 2 \times 1280 + 1$. This corresponds to an average distance $d = 2.03\Delta x$ between two neighbouring point sources. It corresponds to about four points per wavelength for the S wave that is below the minimum number of points per wavelength needed to accurately model propagation of S waves with the FD method. In this situation, we see that some energy is leaking out of the mirror resulting in a significant error affecting the regenerated wavefield. When comparing the snapshots in Figs 10(c) and (d), we observe that varying the number of point sources used to construct the mirror permits to tune the accuracy of the regenerated wavefield.

5.5 On the use of numerical mirrors for the fast computation of synthetic seismograms

In Fig. 11, we show that the time-reversal mirror tool, when it is used to regenerate wavefields going forward in time, permits to efficiently compute the seismic response of a medium that has been
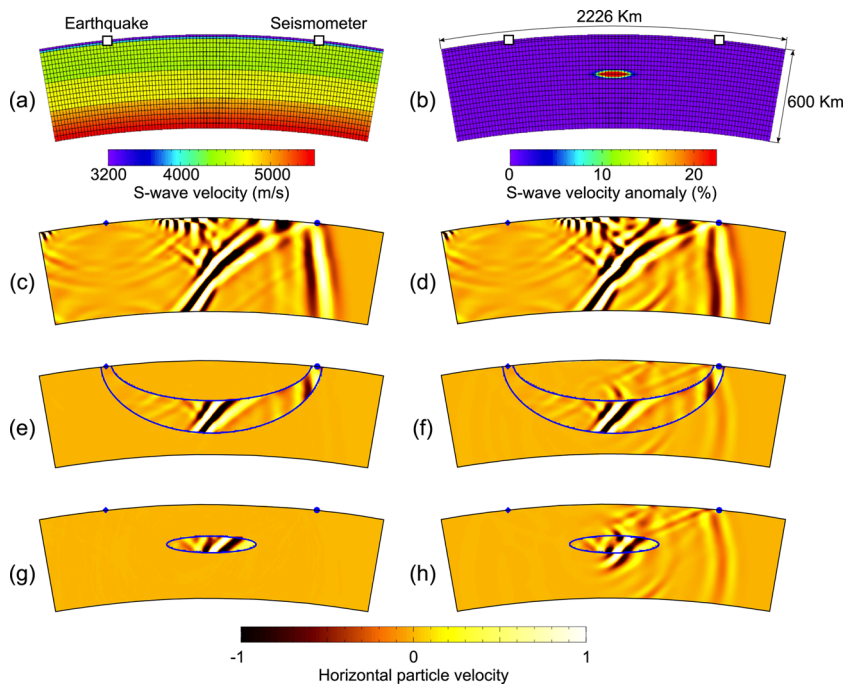

Figure 11. Snapshots of the wavefield following an earthquake computed in a piece of Earth using a 2-D SEM method. The model spans 20 degrees and extends from the surface of the Earth to a depth of 600 km. It is divided into 6090 elements. Inside the elements, the solution is approximated using fourth-order polynomials. The numerical mesh allows to accurately propagate waves with periods greater than 10 s. The source time function has a central frequency $f_c = 1/25$ Hz, the total duration of the simulations is $3000\Delta t$, where, $\Delta t = 0.17$ s. All the snapshots presented have been taken at time $t = 1200\Delta t$. We used absorbing boundaries, on the left, right and bottom side of the model, and a free surface on the top side. (a) Shear-wave velocity in the PREM model. (b) Shear-wave velocity anomaly that is added to the PREM model when computing the response in a perturbed model. (c) Snapshot of the wavefield observed after an earthquake as modelled in the forward simulation. (d) Is similar to (c) but using the perturbed model obtained by adding the anomaly in (b) to the PREM model in (a). (e) Wavefield regenerated forward in time inside a mirror having a tunnel shape. (f) Same as in (e) but using the perturbed model. (g) Wavefield regenerated forward in time inside a mirror having an ellipsoidal shape. (h) Same as in (g) but using the perturbed model.

perturbed locally as proposed by Robertsson & Chapman (2000) and Robertsson *et al.* (2000).

Fig. 11(a) shows the computational domain as well as the reference earth model used for the 2-D SEM simulations. The model spans 20 degrees and extends from the surface of the Earth's to a depth of 600 km. it is divided into 6090 elements delimited by solid lines. Inside the elements, the solution is approximated using fourth-order polynomials. The numerical mesh allows to accurately propagate waves with periods greater than 10 s. The velocity model employed is the PREM model (Dziewonski *et al.* 1981).

Fig. 11(b) represents a velocity anomaly that is added to the reference model in Fig. 11(a) to model wave propagation in a locally perturbed model.

Fig. 11(c) shows the wavefield following an earthquake computed using the reference model in Fig. 11(a). The source time function has a central frequency $f_c = 1/25$ Hz, the total duration of the simulations is $3000\Delta t$, where $\Delta t = 0.17$ s. The snapshot has been taken at time $t = 1200\Delta t$. We used absorbing boundaries, on the left, right and bottom side of the model, and a free surface on the top side.

Fig. 11(d) is similar to Fig. 11(c) but the earth model has been perturbed by adding the anomaly in Fig. 11(b) to the reference model in Fig. 11(a). When comparing Fig. 11(d) to Fig. 11(c) we observe additional scattered waves that are due to the presence of the anomaly.

Fig. 11(e) shows the local regeneration of the wavefield pictured in Fig. 11(c) inside a subvolume having a tunnel shape and going forward in time. To inject the wavefield inside the subvolume, we implemented a time reversal mirror using the direct differentiation method (see Section 4.2). The model employed to model wave propagation is the reference model in Fig. 11(a) and we observe a perfect reconstruction of the original wavefield, that is the obtained wavefield is exactly equal to the wavefield in Fig. 11(c) inside the subvolume delimited by the mirror and zero outside.

Fig. 11(f) has been obtained using the same procedure as in Fig. 11(e), but, the perturbed model in Fig. 11(b) has been used instead of the reference model in Fig. 11(a) when modelling wave propagation. In this case, we observe additional scattered waves due to the presence of the anomaly. Because these waves are not part of the original wavefield, they are not cancelled out when they cross the time-reversal mirror and some energy is leaking out of the subvolume. In fact, inside the subvolume, the regenerated wavefield is exactly equal to the wavefield in Fig. 11(d), while, outside the subvolume, the observed residual is exactly the difference the between the wavefield computed in the perturbed model (in Fig. 11d) and the wavefield computed in the reference model (in Fig. 11c).

Figs 11(g) and (h) have been obtained exactly as Figs 11(e) and (f), respectively. The only difference is that the time-reversal mirror used to regenerate the wavefield has an ellipsoidal shape.

Figs 11(f) and (h) illustrate the fact that, the ability to model the response in a locally perturbed model using the time-reversal mirror has important applications as it allows to restrict the computational domain to the volume inside the mirror. For example one can efficiently compute the response in multiple models that are similar outside the mirror but different inside. This, by using the time-reversal mirror to inject the wavefield recorded in the unperturbed model inside the region where the model has been perturbed. One can use, for example, absorbing boundaries outside the mirror to isolate the computational domain inside the mirror.

In the situation where the sources and the receivers are located inside the mirror as in Fig. 11(e), one directly obtains the response corresponding to the perturbed model. The only part of the signal

that is lost corresponds to the wavefield that escapes the mirror and that is backscattered inside the mirror. These may be considered as second or higher order effects if the dimension of the mirror is appropriate. For example, the shape of the tunnel mirror in Fig. 11(e) may be obtained based on the sensitivity kernel associated with a given seismic wave. Note that exact results could be obtained by modifying the time-reversal mirror as proposed by van Manen *et al.* (2007).

In the situation where the sources and/or the receivers are located outside the volume enclosed in the mirror as in Fig. 11(g), one can record the residual wavefield on the surface of the mirror and use a wavefield extrapolation method to obtain the seismic response at the receivers (e.g. Robertsson & Chapman 2000). The big advantage of this approach is that the wavefield in the complete unperturbed model only needs to be computed once. Moreover, the response of the unperturbed model may be computed using a method that is different from the one used to model the wavefield inside the mirror. In that perspective, the proposed time-reversal mirrors are an efficient tool to develop hybrid methods where a fast solution is used for wave propagation in the larger volume outside the mirror, and an exact method is used inside the mirror.

5.6 Using time reversal mirrors for adjoint tomography

In Fig. 12, we present a time-reversed wavefield obtained using the regional SEM software RegSEM (Cupillard *et al.* 2012). Fig. 12(a) represents the wavefield produced by an earthquake in eastern Europe. The seismic source has coordinates, $45.73°$(latitude), $26.67°$ (longitude), 93.8 Km (depth) and moment tensor

$$\mathbf{M}_0 = \begin{vmatrix} 1.98 & -3.92 & -3.88 \\ -3.92 & 0.77 & 0.005 \\ -3.88 & 0.005 & -2.75 \end{vmatrix} \cdot 10^{-17}. \tag{74}$$

The bandwidth of the source time function goes from 10^{-3} to 10^{-2} Hz. We used the PREM model (Dziewonski & Anderson 1981) to define the velocities and the attenuation inside the propagating medium.

The time-reversal mirror is implemented using the direct discrete differentiation method and follows the faces of the elements to minimize the disk space usage. In the time-reversed simulation, presented in Fig. 12, the wavefield has been amplified to undo the attenuation affecting the wavefield in the forward simulation. To keep the time-reversed simulation stable, we used a point matching technique where the wavefield is reset periodically every 1000 time steps. As the numerical error is growing with time, when amplifying the wavefield in the time-reversed simulation, the regenerated wavefield is less accurate compared to the purely elastic case. Still, the checkpointing technique permits to limit the error and nearly perfect results can be obtained. The time-reversed simulation in Fig. 12(b) can typically be run in parallel with an adjoint simulation (i.e. where we back propagate the misfit between the observed seismograms and the seismogram computed in the current model) to compute sensitivity kernels.

6 CONCLUSION

We introduced two different methods to construct numerical equivalents of time-reversal mirrors. The first method is based on the direct discrete differentiation of the original wavefield. The second method approximates the surface integrals in the Helmoltz-Kirchhoff representations using a set of point sources. Both methods allow us to
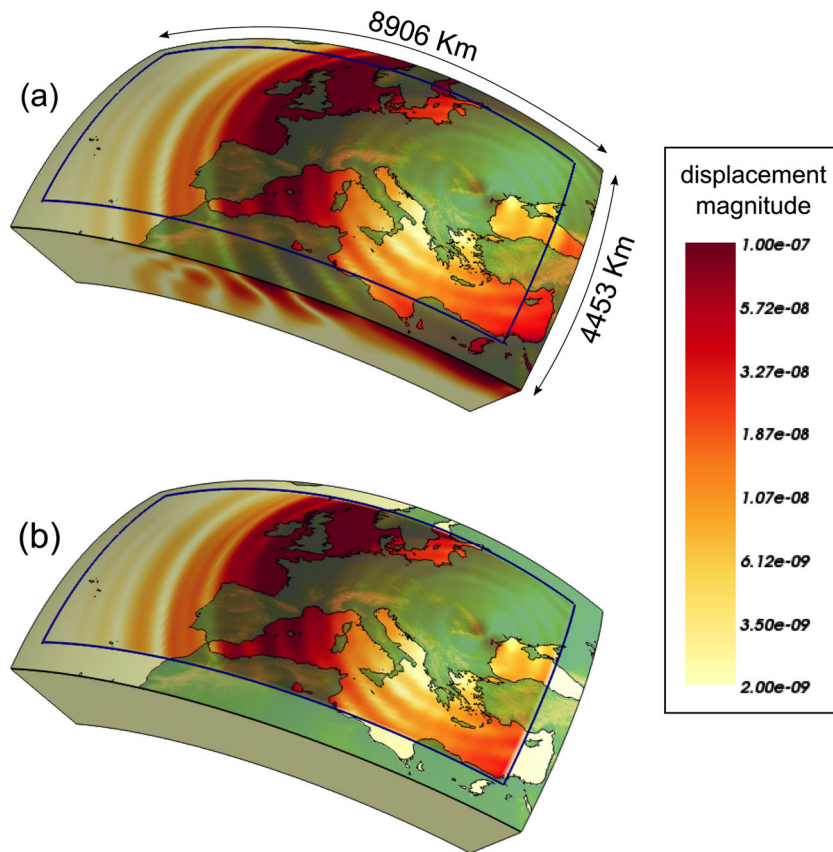
Figure 12. Numerical example of a time-reversed simulation as it can be used, for example, in regional adjoint tomography. The magnitude of the displacement wavefield produced by an earthquake in eastern Europe is pictured. The seismic source has coordinates, 45.73°(latitude), 26.67° (longitude), 93.8 Km (depth). The bandwidth of the source time function goes from 10^{-3} to 10^{-2} Hz. We used the PREM model (Dziewonski & Anderson 1981) to define the velocities and the attenuation inside the propagating medium. (a) Snapshot of wavefield observed after an earthquake in eastern europe modelled using the RegSEM SEM software. Note that the displacement magnitude is pictured using a logarithmic colour scale. (b) Time-reversed simulation where the wavefield in (a) is regenerated locally thanks to the time-reversal mirror.

regenerate an original wavefield locally inside a confined volume surrounded by the time-reversal mirror. The wavefield can be regenerated equally going forward in time or backward in time. The direct discrete differentiation method is perfectly accurate and requires to store the values of the original wavefield at some specific grid points. The multiple point source method is less grid dependent in the sense that the point sources can be placed off the grid nodes. While the accuracy of the multiple point source method is inferior compared to the one of the direct discrete differentiation method, it can be tuned by varying the number of point sources used to approximate the continuous integrals. We showed that the proposed time-reversal mirrors can be used to efficiently model the seismic response in a medium that has been perturbed locally. This opens the possibility to use the proposed mirrors to develop hybrid techniques where different methods are used to model wave propagation inside and outside the mirror. The present study is part of a more general effort to achieve regional scale adjoint tomography in the deep Earth.

ACKNOWLEDGEMENTS

REFERENCES

Akcelik, V. *et al.*, 2003. High resolution forward and inverse earthquake modeling on terascale computers, in *Proceedings of the 2003 ACM/IEEE Conference on Supercomputing,* IEEE, pp. 52–52.

Aki, K. & Richards, P.G., 1980. *Quantitative Seismology,* Vol. 1424, Freeman.

Alterman, Z. & Karal, F., 1968. Propagation of elastic waves in layered media by finite difference methods, *Bull. seism. Soc. Am.,* **58**(1), 367–398.

Bamberger, A., Chavent, G., Hemon, C. & Lailly, P., 1982. Inversion of normal incidence seismograms, *Geophysics,* **47**(5), 757–770.

Baysal, E., Kosloff, D.D. & Sherwood, J.W., 1983. Reverse time migration, *Geophysics,* **48**(11), 1514–1524.

Bednar, J.B., Bednar, C.J. & Shin, C.B., 2006. Two-way vs one-way: a case study style comparison, in *Proceedings of the SEG Annual Meeting,* Society of Exploration Geophysicists, New Orleans, LA.

Bielak, J., 1984. On the effective seismic input for non-linear soil-structure interaction systems, *Earthq. Eng. Struct. Dyn.,* **12,** 107–119.

Bielak, J., Loukakis, K., Hisada, Y. & Yoshimura, C., 2003. Domain reduction method for three-dimensional earthquake modeling in localized regions, part I: theory, *Bull. seism. Soc. Am.,* **93**(2), 817–824.

Biondi, B. & Shan, G., 2002. Prestack imaging of overturned reflections by reverse time migration, in *Proceedings of the SEG Technical Program, Expanded Abstracts,* Vol. 21, pp. 1284–1287.

Bouchon, M. & Sánchez-Sesma, F.J., 2007. Boundary integral equations and boundary elements methods in elastodynamics, *Adv. Geophys.,* **48,** 157–189.

Capdeville, Y., Vilotte, J. & Montagner, J., 2002. Coupling the spectral element method with a modal solution for elastic wave propagation in global earth models, *Geophys. J. Int.,* **152**(1), 34–67.

Capdeville, Y., To, A. & Romanowicz, B., 2003. Coupling spectral elements and modes in a spherical earth: an extension to the sandwichcase, *Geophys. J. Int.,* **154**(1), 44–57.

Capdeville, Y., Guillot, L. & Marigo, J.-J., 2010a. 1-D non-periodic homogenization for the seismic wave equation, *Geophys. J. Int.,* **181**(2), 897–910.

Capdeville, Y., Guillot, L. & Marigo, J.-J., 2010b. 2-D non-periodic homogenization to upscale elastic media for p–sv waves, *Geophys. J. Int.,* **182**(2), 903–922.

Capdeville, Y., Stutzmann, É., Wang, N. & Montagner, J.-P., 2013. Residual homogenization for seismic forward and inverse problems in layered media, *Geophys. J. Int.,* **194**(1), 470–487.

Cassereau, D. & Fink, M., 1992. Time-reversal of ultrasonic fields. III. Theory of the closed time-reversal cavity, *IEEE Trans. Ultrason., Ferroelectr. Freq. Control,* **39**(5), 579–592.

Chen, P, 2011. Full-wave seismic data assimilation: theoretical background and recent advances, *Pure appl. Geophys.,* **168**(10), 1527–1552.

Chen, P., Zhao, L. & Jordan, T.H., 2007. Full 3D tomography for the crustal structure of the los angeles region, *Bull. seism. Soc. Am.,* **97**(4), 1094–1120.

Clapp, R.G., 2009. Reverse time migration with random boundaries, in *Proceedings of the 79th Annual International Meeting, SEG Expanded Abstracts,* Vol. 28, pp. 2809–2813.

Cupillard, P., Delavaud, E., Burgos, G., Festa, G., Vilotte, J.-P., Capdeville, Y. & Montagner, J.-P., 2012. RegSEM: a versatile code based on the spectral element method to compute seismic wave propagation at the regional scale, *Geophys. J. Int.,* **188**, 1203–1220.

De Hoop, A.T., 1958. *Representation Theorems for the Displacement in an Elastic Solid and Their Application to Elastodynamic Diffraction Theory,* Uitgevij Excelsior.

Dumbser, M., Käser, M. & De La Puente, J., 2007. Arbitrary high-order finite volume schemes for seismic wave propagation on unstructured meshes in 2D and 3D, *Geophys. J. Int.,* **171**(2), 665–694.

Dziewonski, A.M. & Anderson, D.L., 1981. Preliminary reference earth model, *Phys. Earth planet. Inter.,* **25**(4), 297–356.

Faccioli, E., Maggio, F., Paolucci, R. & Quarteroni, A., 1997. 2D and 3D elastic wave propagation by a pseudo-spectral domain decomposition method, *J. Seismol.,* **1**(3), 237–251.

Fannjiang, A.C., 2009. On time reversal mirrors, *Inv. Prob.,* **25**(9), 095010.

Fichtner, A., 2010. *Full Seismic Waveform Modelling and Inversion,* Springer.

Fichtner, A., Bunge, H.-P. & Igel, H., 2006. The adjoint method in seismology: I. Theory, *Phys. Earth planet. Inter.,* **157**(1), 86–104.

Fichtner, A., Kennett, B.L., Igel, H. & Bunge, H.-P., 2009. Full seismic waveform tomography for upper-mantle structure in the australasian region using adjoint methods, *Geophys. J. Int.,* **179**(3), 1703–1725.

Fichtner, A., Trampert, J., Cupillard, P., Saygin, E., Taymaz, T., Capdeville, Y. & Villaseñor, A., 2013. Multiscale full waveform inversion, *Geophys. J. Int.,* **194**(1), 534–556.

Fink, M., 1992. Time reversal of ultrasonic fields: I. Basic principles, *IEEE Trans. Ultrason., Ferroelectr. Freq. Control,* **39**(5), 555–566.

Fink, M., 1997. Time reversed acoustics, *Phys. Today,* **50**, 34.

Fink, M. & Prada, C., 2001. Acoustic time-reversal mirrors, *Inv. Prob.,* **17**(1), R1.

Fink, M., Prada, C., Wu, F. & Cassereau, D., 1989. Self focusing in inhomogeneous media with time reversal acoustic mirrors, in *Proceedings of the 1989 IEEE Trans. on Ultrasonics Symposium,* IEEE, pp. 681–686.

Fletcher, R.P. & Robertsson, J.O., 2011. Time-varying boundary conditions in simulation of seismic wave propagation, *Geophysics,* **76**(1), A1–A6.

French, S., Lekić, V. & Romanowicz, B., 2013. Waveform tomography reveals channeled flow at the base of the oceanic asthenosphere, *Science,* **342**(6155), 227–230.

Gauthier, O., Virieux, J. & Tarantola, A., 1986. Two-dimensional nonlinear inversion of seismic waveforms; numerical results, *Geophysics,* **51**(7), 1387–1403.

Godinho, L., Mendes, P.A., Tadeu, A., Cadena-Isaza, A., Smerzini, C., Sánchez-Sesma, F., Madec, R. & Komatitsch, D., 2009. Numerical simulation of ground rotations along 2D topographical profiles under the incidence of elastic plane waves, *Bull. seism. Soc. Am.,* **99**(2B), 1147–1161.

Griewank, A. & Walther, A., 2000. Algorithm 799: revolve: an implementation of checkpointing for the reverse or adjoint mode of computational differentiation, *ACM Trans. Math. Software,* **26**(1), 19–45.

Hinze, M., Walther, A. & Sternberg, J., 2005. An optimal memory-reduced procedure for calculating adjoints of the instationary navier-stokes equations, *Opt. Control Appl. Methods,* **27**(1), 19–40.

Hughes, T.J.R., 1987. *The Finite Element Method, Linear Static and Dynamic Finit Element Analysis,* Prentice–Hall International.

Komatitsch, D., 1997. Méthodes spectrales et éléments spectraux pour l'équation de l'élastodynamique 2 D et 3 D en milieu hétérogène, *PhD thesis*.

Larmat, C., Montagner, J.-P., Fink, M., Capdeville, Y., Tourin, A. & Clévédé, E., 2006. Time-reversal imaging of seismic sources and application to the great sumatra earthquake, *Geophys. Res. Lett.,* **33**(19), doi:10.1029/2006GL026336.

Larmat, C., Tromp, J., Liu, Q. & Montagner, J.-P., 2008. Time reversal location of glacial earthquakes, *J. geophys. Res.,* **113**(B9), B09314, doi:10.1029/2008JB005607.

Lekić, V. & Romanowicz, B., 2011. Inferring upper-mantle structure by full waveform tomography with the spectral element method, *Geophys. J. Int.,* **185**(2), 799–831.

Levander, A., 1988. Fourth-order finite-difference pw seismograms, *Geophysics,* **53**(11), 1425.

Liu, Q. & Tromp, J., 2006. Finite-frequency kernels based on adjoint methods, *Bull. seism. Soc. Am.,* **96**(6), 2383–2397.

Liu, Q. & Tromp, J., 2008. Finite-frequency sensitivity kernels for global seismic wave propagation based upon adjoint methods, *Geophys. J. Int.,* **174**(1), 265–286.

Maday, Y. & Patera, A.T., 1989. Spectral element methods for the incompressible navier-stokes equations, in *Proceedings of the State-of-the-Art Surveys on Computational Mechanics (A90-47176 21-64)*. New York, American Society of Mechanical Engineers, 1989, Vol. 1, pp. 71–143. Research supported by DARPA.

Mittet, R., 1994. Implementation of the kirchhoff integral for elastic waves in staggered-grid modeling schemes, *Geophysics,* **59**(12), 1894–1901.

Moczo, P., Bystrický, E., Kristek, J., Carcione, J.M. & Bouchon, M., 1997. Hybrid modeling of p-sv seismic motion at inhomogeneous viscoelastic topographic structures, *Bull. seism. Soc. Am.,* **87**(5), 1305–1323.

Moczo, P., Kristek, J., Vavryčuk, V., Archuleta, R.J. & Halada, L., 2002. 3D heterogeneous staggered-grid finite-difference modeling of seismic motion with volume harmonic and arithmetic averaging of elastic moduli and densities, *Bull. seism. Soc. Am.,* **92**(8), 3042–3066.

Montagner, J.-P., Larmat, C., Capdeville, Y., Fink, M., Phung, H., Romanowicz, B., Clévédé, E. & Kawakatsu, H., 2012. Time-reversal method and cross-correlation techniques by normal mode theory: a three-point problem, *Geophys. J. Int.,* **191**(2), 637–652.

Monteiller, V., Chevrot, S., Komatitsch, D. & Fuji, N., 2013. A hybrid method to compute short-period synthetic seismograms of teleseismic body waves in a 3-d regional model, *Geophys. J. Int.,* **192**(1), 230–247.

Mulder, W.A. & Plessix, R.-E., 2004. A comparison between one-way and two-way wave-equation migration, *Geophysics,* **69**(6), 1491–1504.

Nissen-Meyer, T., Fournier, A. & Dahlen, F.A., 2007. A two-dimensional spectral-element method for computing spherical-earth seismograms: I. Moment-tensor source, *Geophys. J. Int.,* **168**(3), 1067–1092.

Opršal, I., Matyska, C. & Irikura, K., 2009. The source-box wave propagation hybrid methods: general formulation and implementation, *Geophys. J. Int.,* **176**(2), 555–564.

Patera, A.T., 1984. A spectral element method for fluid dynamics: laminar flow in a channel expansion, *J. Comput. Phys.,* **54**(3), 468–488.

Peter, D. *et al.*, 2011. Forward and adjoint simulations of seismic wave propagation on fully unstructured hexahedral meshes, *Geophys. J. Int.,* **186**(2), 721–739.

Plessix, R.-E., 2006. A review of the adjoint-state method for computing the gradient of a functional with geophysical applications, *Geophys. J. Int.,* **167**(2), 495–503.

Pozrikidis, C., 2005. *Introduction to Finite and Spectral Element Methods Using MATLAB,* Chapman & Hall/CRC.

Restrepo, J.M., Leaf, G.K. & Griewank, A., 1998. Circumventing storage limitations in variational data assimilation studies, *SIAM J. Sci. Comput.,* **19**(5), 1586–1605.

Rickers, F., Fichtner, A. & Trampert, J., 2012. Imaging mantle plumes with instantaneous phase measurements of diffracted waves, *Geophys. J. Int.,* **190**(1), 650–664.

Rickers, F., Fichtner, A. & Trampert, J., 2013. The iceland–jan mayen plume system and its impact on mantle dynamics in the north atlantic region: evidence from full-waveform inversion, *Earth planet. Sci. Lett.,* **367,** 39–51.

Robertsson, J.O.A. & Chapman, C.H., 2000. An efficient method for calculating finite-difference seismograms after model alterations, *Geophysics,* **65**(3), 907–918.

Robertsson, J.O.A., Ryan-Grigor, S., Sayers, C.M. & Chapman, C.H., 2000. A finite-difference injection approach to modeling seismic fluid flow monitoring, *Geophysics,* **65**(3), 896–906.

Seriani, G., Priolo, E. & Pregarz, A., 1995. Modelling waves in anisotropic media by a spectral element method, in *Proceedings of the Third International Conference on Mathematical and Numerical Aspects of Wave Propagation,* SIAM, pp. 289–298.

Snieder, R., 2002. General theory of elastic wave scattering, in *Scattering and Inverse Scattering in Pure and Applied Science,* chap. 1.7.1, pp. 528–542, eds Pike, R. & Sabatier, P., Academic Press.

Symes, W.W., 2007. Reverse time migration with optimal checkpointing, *Geophysics,* **72**(5), SM213–SM221.

Tape, C., Qinya, L., Maggi, A. & Tromp, J., 2009. Adjoint tomography of the southern california crust, *Science,* **325**(5943), 988–992.

Tarantola, A., 1984. Inversion of seismic reflection data in the acoustic approximation, *Geophysics,* **49**(8), 1259–1266.

Tarantola, A., 1988. Theoretical background for the inversion of seismic waveforms including elasticity and attenuation, *Pure appl. Geophys.,* **128**(1-2), 365–399.

To, A., Romanowicz, B., Capdeville, Y. & Takeuchi, N., 2005. 3D effects of sharp boundaries at the borders of the African and pacific superplumes: observation and modeling, *Earth planet. Sci. Lett.,* **233**(1), 137–153.

Tromp, J., Tape, C. & Liu, Q., 2005. Seismic tomography, adjoint methods, time reversal and banana-doughnut kernels, *Geophys. J. Int.,* **160**(1), 195–216.

van Manen, D.-J., Robertsson, J. O.A. & Curtis, A., 2007. Exact wave field simulation for finite-volume scattering problems, *J. Acoust. Soc. Am.,* **122**(4), EL115–EL121.

Virieux, J., 1986. P-sv wave propagation in heterogeneous media; velocity-stress finite-difference method, *Geophysics,* **51**(4), 889–901.

Wen, L. & Helmberger, D.V., 1998. A two-dimensional P-SV hybrid method and its application to modeling localized structures near the core-mantle boundary, *J. geophys. Res.,* **103**(B8), 17901–17918.

Whitmore, N., 1983. Iterative depth migration by backward time propagation, in *Proceedings of the 1983 SEG Annual Meeting,* Society of Exploration Geophysicists, Las Vegas, NV.

Yee, K., 1966. Numerical solution of initial boundary value problems involving Maxwell's equations in isotropic media, *IEEE Trans. Anten. Propag.,* **14**(3), 302–307.

Yoon, K., Shin, C., Suh, S., Lines, L.R. & Hong, S., 2003. 3d reverse-time migration using the acoustic wave equation: an experience with the seg/eage data set, *Lead. Edge,* **22**(1), 38–41.

Yoon, K., Marfurt, K.J. & Starr, W., 2004. Challenges in reverse-time migration, in *Proceedings of the 2004 SEG Annual Meeting,* Society of Exploration Geophysicists, Denver, CO.

Yoshimura, C., Bielak, J., Hisada, Y. & Fernández, A., 2003. Domain reduction method for three-dimensional earthquake modeling in localized regions, part II: verification and applications, *Bull. seism. Soc. Am.,* **93**(2), 825–841.

Zhao, L., Wen, L., Chen, L. & Zheng, T., 2008. A two-dimensional hybrid method for modeling seismic wave propagation in anisotropic media, *J. geophys. Res.,* **113**(B12), B12307, doi:10.1029/2008JB005733.

Zhu, H., Bozdağ, E., Peter, D. & Tromp, J., 2012. Structure of the european upper mantle revealed by adjoint tomography, *Nat. Geosci.,* **5**(7), 493–498.